Mechanical Systems and Signal Processing 243 (2026) 113704

Contents lists available at ScienceDirect

Mechanical Systems and Signal Processing

journal homepage: www.elsevier.com/locate/ymssp

Full Length Article

Periodic and aperiodic hierarchical chiral metamaterials for broadband vibration suppression

Dewen Yu [a,b], Qiangqiang Zhao [b,*], Gang Wang [b], Guobiao Hu [c], Haoxiang Xi [b], Baiyi Li [b], Jun Hong [b]

[a] Frontier Institute of Science and Technology, Xi'an Jiaotong University, Xi'an 710049, China
[b] Key Laboratory of Education Ministry for Modern Design and Rotor-Bearing System, School of Mechanical Engineering, Xi'an Jiaotong University, Xi'an 710049, China
[c] Internet of Things Thrust, The Hong Kong University of Science and Technology (Guangzhou), Guangzhou 511400, China

ARTICLE INFO

Communicated by Dr Ji JC

Keywords:
Hierarchical chiral metamaterial
Broadband vibration suppression
Aperiodic design
Band gap
Spectral element method

ABSTRACT

While chiral metamaterials excel in wave manipulation, their potential for low-frequency broadband vibration suppression remains underexplored. This study proposes a new design paradigm that integrates the principles of "tacticity" and "hierarchy" into chiral lattices. Eight hierarchical chiral elementary cells with self-similar geometry are assembled to construct periodic and aperiodic metamaterials, enabling reduced starting frequencies of band gaps at an identical stiffness-mass ratio. To facilitate the customization design, a theoretical framework is established for predicting the transmittance spectra and band structure of these hierarchical chiral metamaterials, which is validated through simulational results and experimental tests. It is demonstrated that the periodic syndiotactic metamaterial generates two wide band gaps, the normalized starting frequency of which is lower than that observed in non-hierarchical, mono-hierarchical, and de-chiralized reference configurations. The intrinsic band gap formation mechanisms are elucidated, and a systematic parametric analysis is conducted to guide band gap tailoring. Furthermore, through the combinatorial optimization of topological configurations and structural parameters, the resulting aperiodic hierarchical chiral metamaterial achieves superior broadband vibration suppression performance. Compared to the periodic configuration, the aperiodic design not only broadens the initial band gap by 122.2 % but also reduces the starting frequency by 34.4 %. Overall, the tacticity-hierarchy framework and theoretical model developed in this work provide a general pathway to engineer customizable, low-frequency, broadband band gaps for vibration suppression.

1. Introduction

Mechanical metamaterials [1–3], characterized by engineered artificial morphology and tailored physical properties [4], enable the elastic wave manipulation [5] across extensive frequency ranges and at deep subwavelength scales [6]. This capability has driven substantial research interest over the past decades [7–9]. Beyond their anomalous dynamic properties, a prominent feature of these mechanical metamaterials is the emergence of band gaps [10–12], in which vibration transmission is significantly attenuated

* Corresponding author.
E-mail address: qzhao21@xjtu.edu.cn (Q. Zhao).

https://doi.org/10.1016/j.ymssp.2025.113704
Received 25 August 2025; Received in revised form 13 November 2025; Accepted 28 November 2025
Available online 4 December 2025

throughout the architected structure [13].

The band gap properties of metamaterials are mainly attributed to the structural design of their microstructure rather than their constituent materials [14–16]. The design methodologies are typically based on two fundamental mechanisms of band gap formation: Bragg scattering [17,18] and local resonant [19,20]. Since the Bragg scattering occurs at an elastic wavelength compatible with the periodic length, the locally resonant metamaterials are preferred for low-frequency vibration suppression, but the latter suffers from limited and dispersed bandwidth. Recently, inertial amplification [21–23] has emerged as a promising strategy to generate broad low-frequency band gaps within lightweight mechanical metamaterials. In addition, quasi-zero stiffness metamaterials [24,25] can open ultra-low frequency band gaps, but their effective operational range for vibration isolation is narrow and highly sensitive to the load-mass deviation [26]. Moreover, regarding the metamaterial design, a significant realization barrier arises from the fabrication complexities of intricate architectures [27,28], generally leading to impractical production challenges or structural fragility failure [29]. Therefore, balancing the competing demands of light weight, high stiffness, simple geometry, and low-frequency broadband performance remains to be further explored.

Within this context, chirality-inspired periodic metamaterials are drawing more and more attention [30–33] due to their unique mechanical performance [34,35], including the compression-torsion coupling effect [36,37] and inertial amplification effect [38,39]. In contrast to ordinary geometry configurations, chirality breaks the structural symmetry, thereby enabling the creation of elastic wave band gaps within the metamaterials [40–42]. Bergamini et al. [43] found that the relative orientation of adjacent chiral cells significantly impacts their vibrational transmission responses. After exploring the band gap phenomena through an analogy with Thomson scattering [44], Ding et al. [45] introduced spherical hinges into the chiral metamaterial to alleviate the mutual constraint between the start frequency and bandwidth. Park et al. [46] successfully achieved low-frequency multimodal wave attenuation in chiral trabeated metabeams by overlapping the flexural and longitudinal-torsional band gaps. Furthermore, Zhang et al. [47] embedded local resonators into the chiral metamaterials to trigger lower frequency band gaps. Through integrating the tunable rudder oscillators into chiral structures, Yu et al. [48] manipulated the band gap properties of chiral metamaterials while preserving their original support stiffness and total weight. Despite these studies enriching band gap properties, the structural designs largely remain anchored in classic chiral topologies. Thus, developing more advanced design paradigms is desired to fully unlock the potential of chirality-inspired metamaterials for band gap enhancement and on-demand customization [30].

In practice, the design of metamaterial micro-architectures for the desired performance is often intractable [49,50], as it requires accurate correlation between dynamic response and structural topology [51–53]. The prevailing strategy simplifies this complexity by imposing periodicity with identical unit cells, but it sacrifices the achievable spectrum of physical properties [54]. In response, considerable efforts seek to alleviate this limitation by enhancing micro-architectural heterogeneity or dissimilarity within the periodic unit [55–58]. For example, Abdeljaber et al. [59] identified optimal geometric parameters of graded chiral lattices for vibration suppression. Fundamentally, the gradient design strategy achieves broadband wave control through spatial segregation of local resonator frequencies, but this inherently diminishes attenuation intensity within the resultant band gaps [60]. Drawing inspiration from spatial parameter modulation, mechanical metamaterials with the rainbow trapping effect [61,62] and stiffness-mass-coding design [63] have also been developed to customize band gaps. For instance, Li et al. [64] demonstrate that the band gaps of membrane-type metamaterials can be significantly widened through strategic selection of parameter combinations. In addition, Poggetto et al. [65] integrated the hierarchical architecture into periodic frames to broaden the band gaps of elastic waves. While fractal hierarchical periodic structures enhance the multiplicity and overall bandwidth of band gaps, the unclear coupling mechanism between the dispersion relation and structural hierarchy may inadvertently introduce undesirable passbands, narrowing the individual width of lower-frequency band gaps [66].

It is noteworthy that the gradient and hierarchical design strategies described above only enrich the irregularity of unit cells, while the metamaterial structures still feature strict periodicity. In contrast, wave propagation in non-periodic metamaterials manifests more intriguing phenomena [67–69]. Studies have shown that the quasicrystal structures or aperiodic configurations exhibit unique energy localization [70,71], wave reflection [72,73], and band formation [74,75]. Based on these findings, a natural hypothesis is that breaking the periodic arrangement or utilizing disordered resonators could be an effective strategy to mitigate wave amplification. On the other hand, abrupt geometrical variations between adjacent units significantly influence the low-frequency elastic wave propagation [59,76], potentially eliminating attenuation regions or shortening bandwidth [66,77]. Hence, deterministic aperiodic metamaterials with extensive reconfigurable configurations formed by simple elementary cells remain scarce for continuous and broadband vibration suppression.

Motivated by the above-mentioned research gaps, this work presents a novel class of periodic and aperiodic hierarchical chiral metamaterials to improve the vibration suppression performance. By exploiting the augmented design freedom from multiple chirality, we demonstrate that rationally engineered aperiodic variants outperform their periodic counterparts in achieving continuous and broadband vibration suppression.

The main contributions of this study are threefold. (1) Through the innovative synthesis of “tacticity” and “hierarchy”, eight chiral elementary cells with self-similar geometry are designed to construct periodic and aperiodic metamaterials, allowing for reducing the start frequency at identical stiffness-mass ratios. (2) Unlike stochastic metamaterials generated from random or selective representations [78,79], our hierarchical design strategy yields deterministic aperiodic fabrication-friendly metastructures, whose band gaps can be precisely manipulated by adjusting both chirality arrangements and local shapes. (3) Different from conventional co-simulation techniques using finite element software [51,80], a function-based modeling approach is developed to efficiently solve the inverse optimization problem, determining the optimal configuration from the desired behavior by selecting appropriate elementary cells with fine-tuned structural parameters.

Subsequent contents are organized as follows. To start with, the design concept and the architectural configuration of hierarchical

chiral metamaterials are elucidated in Section 2. Section 3 establishes a theoretical formulation for predicting the vibration propagation behavior. Section 4 validates this theoretical model via simulation results and experimental tests. Section 5 discusses the vibration suppression performance of periodic hierarchical chiral metamaterials. Furthermore, Section 6 demonstrates the superiority of aperiodic metamaterials in broadband vibration suppression. Finally, Section 7 summarizes the concluding remarks of this research.

2. Geometrical configuration design

Focusing on the intrinsic correlation between structure and performance, the design concept of hierarchical chiral metamaterials will be presented in this section. Through the integration of "tacticity" and "hierarchy", the proposed design strategy seeks to widen the band gaps while retaining the original specific stiffness. Simultaneously, the abundance of elementary cells endows the metamaterials with intriguing capabilities for elastic wave manipulation.

Given the merits of the compression-torsion coupling effect and inertial amplification effect [36–39], the chiral lattice structure is selected as the basic geometry in this study. As shown in Fig. 1(a), such basic elements are made up of four inclined struts and two substrate plates. Similar to the concept of "tacticity" in polymer chemistry [81], the combination of chirality brings about isotactic, syndiotactic, and atactic configurations. Chemically, isotactic polymers are characterized by a uniform monomer arrangement,

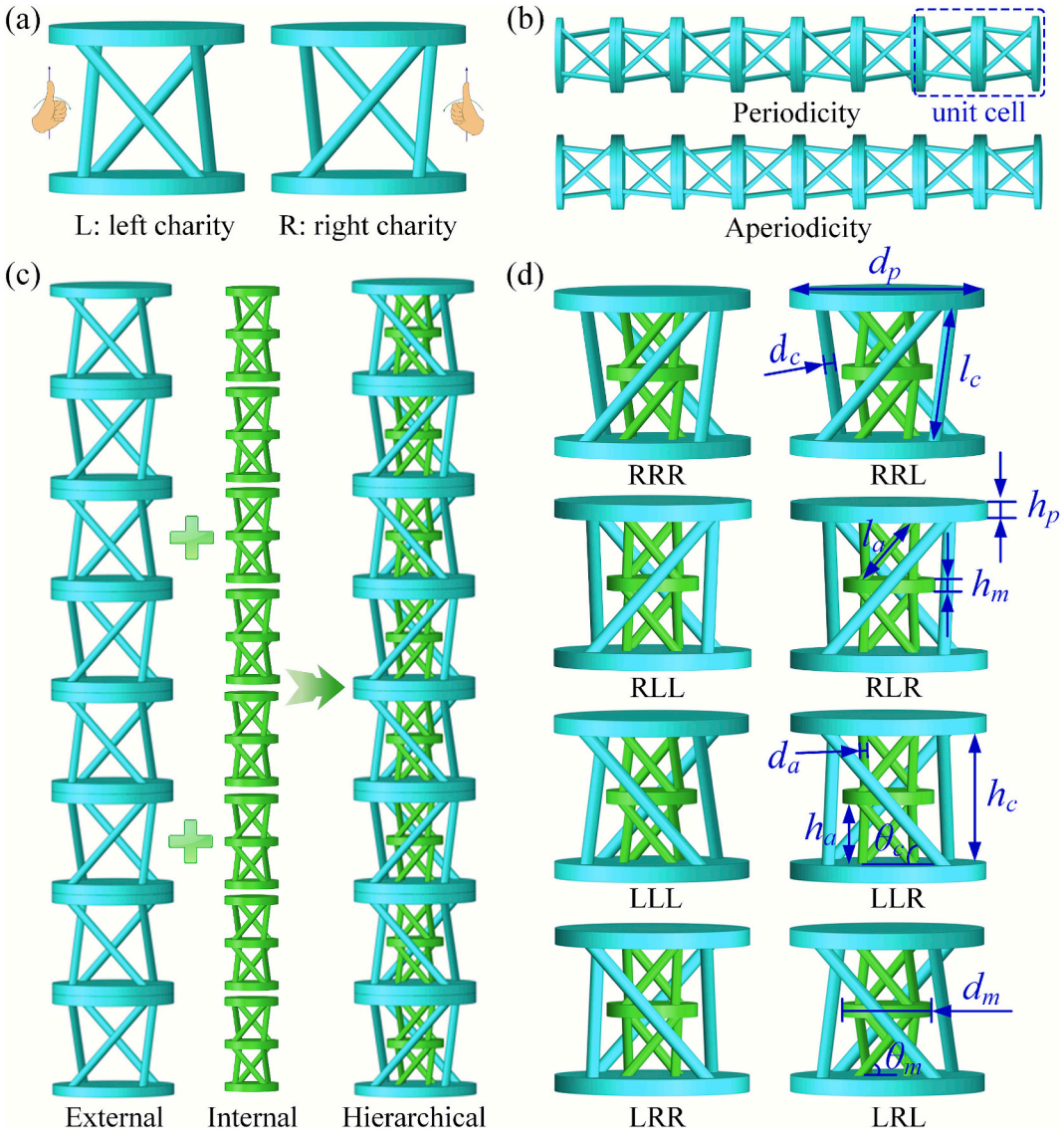

Fig. 1. Schematic diagram of the developed hierarchical chiral metamaterials. (a) Basic left- and right-handed chiral elements; (b) Periodic and aperiodic configurations; (c) Hierarchical nested design with an external chiral frame and internal chiral micro-structures; (d) Eight elementary cells with self-similar geometry for the hierarchical chiral metamaterials.

whereas syndiotactic polymers exhibit a regular alternating pattern. In contrast, atactic polymers display a random monomer distribution without periodicity. By analogy, the elementary cells of metamaterials act as the monomer units in polymers. Moreover, the proposed elementary cells differ only in their chirality, which can be either left- or right-handed. These features contribute to diverse arrangement combinations with geometrical similarity.

Drawing inspiration from the intriguing characteristics of tacticity, we further design the isotactic, syndiotactic, and atactic chiral metamaterials. Specifically, the isotactic configuration exhibits a highly regular pattern in which the unit cells are exclusively left- or right-handed. The syndiotactic configuration, as presented in the upper part of Fig. 1(b), alternates between left- and right-handed chiral elements. In contrast, the atactic form, as depicted in the bottom part of Fig. 1(b), is characterized by the random distribution of its basic elements. Therefore, the isotactic and syndiotactic configurations are periodic, whereas the atactic configuration is aperiodic.

By applying the self-similar principle to nest multiple levels of basic geometrical topology across different size scales, the hierarchical chiral metamaterials are constructed as shown in Fig. 1(c). The external chiral structure primarily serves to provide load-bearing stiffness, while the two chiral micro-structures are integrated into the internal cavity as local resonators to enhance vibration suppression performance. In comparison to single-layer chiral metamaterials, the proposed hierarchical design enables the generation of broader band gaps alongside a superior strength-to-weight ratio. Moreover, as depicted in Fig. 1(d), the introduction of hierarchy enriches the subset of elementary cells, providing more versatility for waveguide manipulation in diverse applications. For clarity, the hierarchy of the elementary cells is characterized by three-letter combinations, such as “RLR”. The first letter denotes the charity of the external structure, while the second and third letters represent the charity of the downward and upward structures in the internal layer, respectively. Herein, the abbreviations “R” and “L” denote right- and left-handed chiral units.

Fig. 1(d) also illustrates the geometric parameters of each elementary cell. For the external chiral frame, the two parallel substrate plates are separated by a distance of h_c, and their diameter and thickness are d_p and h_p, respectively. Four cross-distributed inclined struts with a tilt angle of θ_c are located on the surface of the cuboid interspace, and their length and diameter for these external inclined struts are defined by l_c and d_c, respectively. Regarding the internal chiral structures, the middle substrate plate has a diameter of d_m and

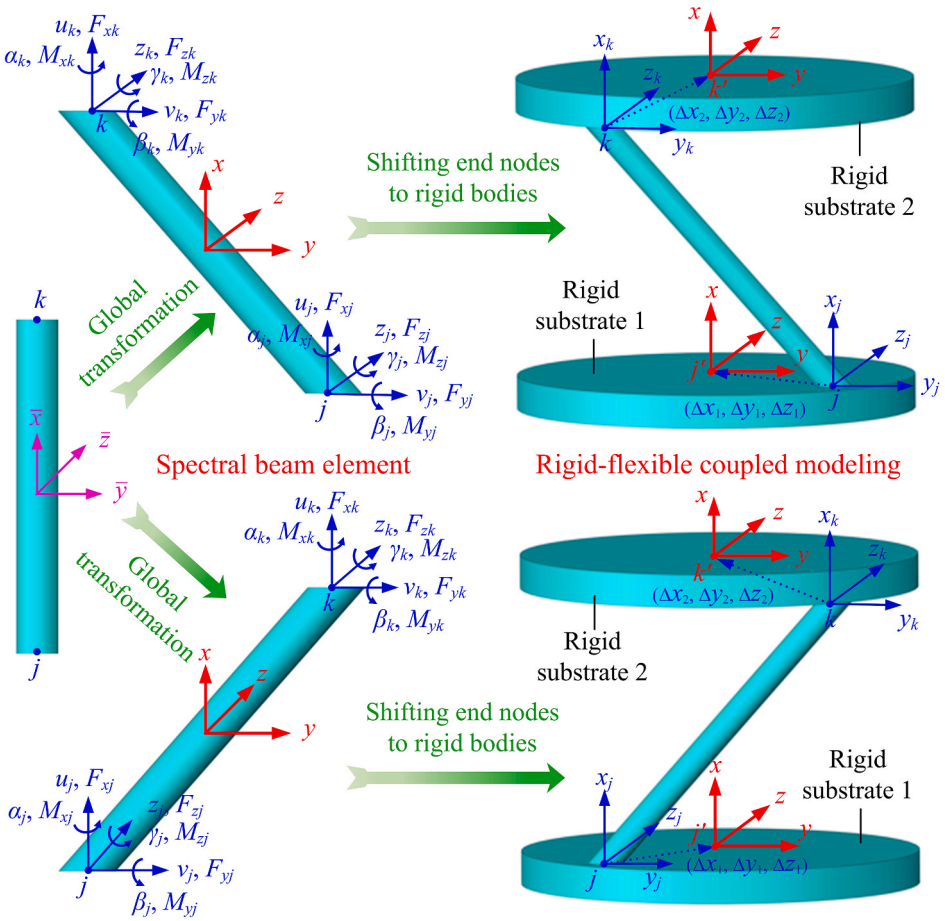

Fig. 2. Kinematic transformation of strut end nodes to connected substrate plates. For the two-node spectral beam element, each node possesses complete translational and rotational degrees of freedom, with nodal forces comprising both force and moment components. The relative displacements from j to j' and from k to k' are $(\Delta x_1, \Delta y_1, \Delta z_1)$ and $(\Delta x_2, \Delta y_2, \Delta z_2)$, respectively.

a thickness of h_m. The length, diameter, and height of internally inclined struts are specified as l_a, d_a, and h_a, respectively, with their tilt angle indicated by θ_m.

3. Theoretical formulation

Accurate prediction of dynamic behavior is indispensable for tailoring band gaps. Toward this end, the dynamic governing equations are derived herein to characterize the vibrational response and reveal the band structure features inherent to hierarchical chiral metamaterials.

3.1. Vibration response modeling with extended dynamic stiffness matrices

Current dynamic modeling techniques include the transfer matrix method (TMM) [82], the lumped mass-spring method (LMSM) [5], the plane wave expansion method (PWEM) [83], the finite element method (FEM) [84], and the spectral element method (SEM) [85]. Among these methods, the TMM is primarily confined to one-dimensional systems, as it struggles with complex structural configurations. Ding et al. [44] applied LMSM to analyze the dynamic response of chiral metamaterials, but the developed model demands a size-dependent correction factor to modify the effective radius. The PWEM requires that the material properties of the periodic medium be formulated in a closed form, thus reducing its versatility. Owing to the availability of commercial software, the FEM has been widely adopted for calculating the vibration response and the deformation modes, but the simulation process is computationally intensive. Different from the FEM that necessitates refined meshes, the SEM enhances the computational efficiency by modeling entire uniform segments using a single element. In light of these facts, the SEM is employed here to develop an efficient theoretical framework for predicting the band gap properties of chiral metamaterials.

Across the frequency domain of interest, deformation in the hierarchical chiral metamaterials is predominantly localized to the support struts, with negligible distortion observed in the substrate plates. This characteristic justifies the rigid-body assumption for the plates. Based on this premise, an extended spectral element method that effectively integrates the synergistic effects of rigid-flexible interaction and compression-torsion coupling is presented here for vibration analysis.

As illustrated in Fig. 2, a spectral beam element formulated in the frequency domain is applied to characterize the dynamic behavior of inclined struts. The nodal force vector $\mathbf{F}_{jk}$ for a strut is determined by the nodal displacement $\mathbf{d}_{jk}$ and the dynamic stiffness matrix $\mathbf{S}_b$, which is expressed as [72]:

$$\begin{cases} \mathbf{F}_{jk} = \mathbf{S}_b \mathbf{d}_{jk} \\ \mathbf{F}_{jk} = \left[\mathbf{F}_j^{\mathrm{T}}, \mathbf{F}_k^{\mathrm{T}}\right]^{\mathrm{T}}, \quad \mathbf{F}_j = \left[F_{xj}, F_{yj}, F_{zj}, M_{xj}, M_{yj}, M_{zj}\right]^{\mathrm{T}}, \quad \mathbf{F}_k = \left[F_{xk}, F_{yk}, F_{zk}, M_{xk}, M_{yk}, M_{zk}\right]^{\mathrm{T}} \\ \mathbf{d}_{jk} = \left[\mathbf{d}_j^{\mathrm{T}}, \mathbf{d}_k^{\mathrm{T}}\right]^{\mathrm{T}}, \quad \mathbf{d}_j = \left[u_j, v_j, w_j, \alpha_j, \beta_j, \gamma_j\right]^{\mathrm{T}}, \quad \mathbf{d}_k = \left[u_k, v_k, w_k, \alpha_k, \beta_k, \gamma_k\right]^{\mathrm{T}} \end{cases} \tag{1}$$

Note that four cross-distributed inclined struts are connected to rigid substrate plates. This geometric configuration implies that the terminal displacement of these flexible struts must conform to the rigid kinematic constraints. Accordingly, as presented in Fig. 2, we will extend the formulation of spectral beam elements to achieve the rigid-flexible coupled modeling.

Given that the relative displacement between nodes j and j' is $(\Delta x_1, \Delta y_1, \Delta z_1)$, the force equilibrium equations and geometric relationships for these two nodes are derived as follows:

$$\begin{cases} F_{xj'} = F_{xj}, & u_{j'} = u_j + \beta_j \Delta z_1 - \gamma_j \Delta y_1 \\ F_{yj'} = F_{yj}, & v_{j'} = v_j - \alpha_j \Delta z_1 + \gamma_j \Delta x_1 \\ F_{zj'} = F_{zj}, & w_{j'} = w_j + \alpha_j \Delta y_1 - \beta_j \Delta x_1 \\ M_{xj'} = M_{xj} + F_{yj} \Delta z_1 - F_{zj'} \Delta y_1, & \alpha_{j'} = \alpha_j \\ M_{yj'} = M_{yj} - F_{xj} \Delta z_1 + F_{zj} \Delta x_1, & \beta_{j'} = \beta_j \\ M_{zj'} = M_{zj} + F_{xj} \Delta y_1 - F_{yj} \Delta x_1, & \gamma_{j'} = \gamma_j \end{cases} \tag{2}$$

The above propagation relation can be reshaped into

$$\mathbf{F}_{j'k} = \mathbf{T}_{11} \mathbf{F}_{jk}, \quad \mathbf{X}_{j'k} = \mathbf{T}_{12} \mathbf{X}_{jk} \tag{3}$$

where the transfer matrices $\mathbf{T}_{11}$ and $\mathbf{T}_{12}$ are determined by

$$\mathbf{T}_{11} = \begin{bmatrix} \mathbf{I}_{3\times3} & \mathbf{0}_{3\times3} & \mathbf{0}_{3\times3} & \mathbf{0}_{3\times3} \\ \boldsymbol{\varpi}_1 & \mathbf{I}_{3\times3} & \mathbf{0}_{3\times3} & \mathbf{0}_{3\times3} \\ \mathbf{0}_{3\times3} & \mathbf{0}_{3\times3} & \mathbf{I}_{3\times3} & \mathbf{0}_{3\times3} \\ \mathbf{0}_{3\times3} & \mathbf{0}_{3\times3} & \mathbf{0}_{3\times3} & \mathbf{I}_{3\times3} \end{bmatrix}, \quad \mathbf{T}_{12} = \begin{bmatrix} \mathbf{I}_{3\times3} & \boldsymbol{\varpi}_1 & \mathbf{0}_{3\times3} & \mathbf{0}_{3\times3} \\ \mathbf{0}_{3\times3} & \mathbf{I}_{3\times3} & \mathbf{0}_{3\times3} & \mathbf{0}_{3\times3} \\ \mathbf{0}_{3\times3} & \mathbf{0}_{3\times3} & \mathbf{I}_{3\times3} & \mathbf{0}_{3\times3} \\ \mathbf{0}_{3\times3} & \mathbf{0}_{3\times3} & \mathbf{0}_{3\times3} & \mathbf{I}_{3\times3} \end{bmatrix}, \boldsymbol{\varpi}_1 = \begin{bmatrix} 0 & \Delta z_1 & -\Delta y_1 \\ -\Delta z_1 & 0 & \Delta x_1 \\ \Delta y_1 & -\Delta x_1 & 0 \end{bmatrix} \tag{4}$$

where $\mathbf{I}_{3\times3}$ and $\mathbf{0}_{3\times3}$ denote the 3×3 identity and zero matrices, respectively.

Following the same procedure, the terminal node k is mapped to node k', which is situated on the other rigid substrate plate. As established in Eq. (3), the conjugate transformations between nodes k and k' are governed by

$$\mathbf{F}_{j'k'} = \mathbf{T}_{21} \mathbf{F}_{j'k}, \quad \mathbf{X}_{j'k'} = \mathbf{T}_{22} \mathbf{X}_{j'k}, \tag{5}$$

where the transfer matrices $\mathbf{T}_{21}$ and $\mathbf{T}_{22}$ are expressed as

$$\mathbf{T}_{21}=\begin{bmatrix}\mathbf{I}_{3\times3} & \mathbf{0}_{3\times3} & \mathbf{0}_{3\times3} & \mathbf{0}_{3\times3}\\ \mathbf{0}_{3\times3} & \mathbf{I}_{3\times3} & \mathbf{0}_{3\times3} & \mathbf{0}_{3\times3}\\ \mathbf{0}_{3\times3} & \mathbf{0}_{3\times3} & \mathbf{I}_{3\times3} & \mathbf{0}_{3\times3}\\ \mathbf{0}_{3\times3} & \mathbf{0}_{3\times3} & \boldsymbol{\varpi}_2 & \mathbf{I}_{3\times3}\end{bmatrix},\quad \mathbf{T}_{22}=\begin{bmatrix}\mathbf{I}_{3\times3} & \mathbf{0}_{3\times3} & \mathbf{0}_{3\times3} & \mathbf{0}_{3\times3}\\ \mathbf{0}_{3\times3} & \mathbf{I}_{3\times3} & \mathbf{0}_{3\times3} & \mathbf{0}_{3\times3}\\ \mathbf{0}_{3\times3} & \mathbf{0}_{3\times3} & \mathbf{I}_{3\times3} & \boldsymbol{\varpi}_2\\ \mathbf{0}_{3\times3} & \mathbf{0}_{3\times3} & \mathbf{0}_{3\times3} & \mathbf{I}_{3\times3}\end{bmatrix},\ \boldsymbol{\varpi}_2=\begin{bmatrix}0 & \Delta z_2 & -\Delta y_2\\ -\Delta z_2 & 0 & \Delta x_2\\ \Delta y_2 & -\Delta x_2 & 0\end{bmatrix} \tag{6}$$

The relative displacement vector $(\Delta x_2,\ \Delta y_2,\ \Delta z_2)$ quantifies nodal positional translation from k to k'.

By integrating Eqs. (3) and (5), the displacement-force propagation relationship at the nodes j' and k' is derived as

$$\mathbf{F}_{j'k'}=\left[(\mathbf{T}_{21}\mathbf{T}_{11})\mathbf{S}_b(\mathbf{T}_{22}\mathbf{T}_{12})^{-1}\right]\mathbf{X}_{j'k'}=\mathbf{D}_b\mathbf{X}_{j'k'} \tag{7}$$

where $\mathbf{D}_b$ denotes the extended dynamic stiffness matrix of the strut, with its end nodes transferred to the adjacent substrate plates.

Upon completing this transformation, the nodes of the four inclined struts are uniformly merged into the centers of the corresponding substrate plates. As illustrated in Fig. 3, the node condensation leads to the reduction of the dynamic stiffness matrix of each basic chiral unit to a 12 × 12 matrix. Given that a hierarchical chiral elementary cell consists of three similar basic chiral units, as depicted in Fig. 3, a modular assembly is first executed, and then the dynamic stiffness matrix of each elementary cell can be readily derived via global assembly.

To facilitate the modular assembly of each elementary cell, the dynamic equation of the n-th basic chiral unit is recast as

$$\begin{bmatrix}\mathbf{F}_{n,j'}\\ \mathbf{F}_{n,k'}\end{bmatrix}=\begin{bmatrix}\mathbf{D}_{n,1} & \mathbf{D}_{n,2}\\ \mathbf{D}_{n,3} & \mathbf{D}_{n,4}\end{bmatrix}\begin{bmatrix}\mathbf{X}_{n,j'}\\ \mathbf{X}_{n,k'}\end{bmatrix} \tag{8}$$

where $\mathbf{X}_{n,j'}$ and $\mathbf{X}_{n,k'}$ denote the nodal displacement vectors at j' and k', respectively, while $\boldsymbol{F}_{n,j'}$ and $\boldsymbol{F}_{n,k'}$ correspond to the resultant force vectors. Additionally, the dynamic stiffness matrix $\mathbf{D}_n$ of the n-th basic chiral unit is partitioned into $\mathbf{D}_{n,1}$, $\mathbf{D}_{n,2}$, $\mathbf{D}_{n,3}$, and $\mathbf{D}_{n,4}$. These variables are all defined in global coordinates.

As depicted in Fig. 3, a hierarchical chiral elementary cell can be characterized by three nodes. According to the D'Alembert principle, the force equilibrium equation for each elementary cell, which incorporates the inertial effect of the substrate plates and the dynamic stiffness of flexible struts, is derived as:

$$\begin{bmatrix}\mathbf{F}_1(\omega)\\ \mathbf{F}_2(\omega)\\ \mathbf{0}_{6\times1}\end{bmatrix}=\begin{bmatrix}\mathbf{D}_{1,\ 1}+\mathbf{D}_{2,\ 1}+\mathbf{M}_p & \mathbf{D}_{1,\ 2} & \mathbf{D}_{2,\ 2}\\ \mathbf{D}_{1,\ 3} & \mathbf{D}_{1,\ 4}+\mathbf{D}_{3,\ 4}+\mathbf{M}_p & \mathbf{D}_{3,\ 3}\\ \mathbf{D}_{2,\ 3} & \mathbf{D}_{2,\ 4}+\mathbf{D}_{3,\ 2}+\mathbf{M}_m & \mathbf{D}_{3,\ 1}\end{bmatrix}\begin{bmatrix}\mathbf{X}_1\\ \mathbf{X}_2\\ \mathbf{X}_3\end{bmatrix} \tag{9}$$

where $\mathbf{F}_1(\omega)$ and $\mathbf{F}_2(\omega)$ are the input and output forces applied on the external chiral frame, respectively; $\mathbf{M}_p$ and $\mathbf{M}_m$ denote the inertial matrices of external and internal substrate plates, respectively; $\mathbf{X}_i$ $(i=1,\ 2,\ 3)$ represents the nodal displacement of the i-th node.

After determining the input–output relationship of each chiral elementary cell, the derivation of the frequency response function for the entire hierarchical chiral metamaterial becomes straightforward due to its cascaded configuration. By imposing the boundary conditions on the governing equation of the system, we can obtain

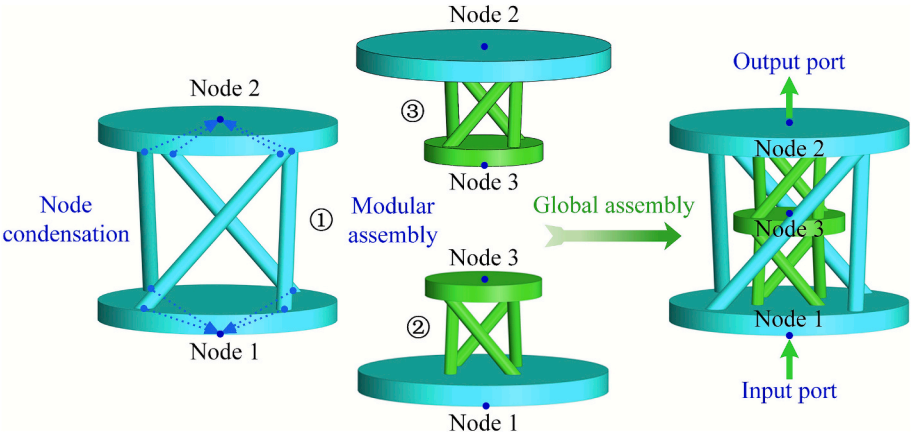

Fig. 3. Construction of the global dynamic stiffness matrix for the hierarchical chiral elementary cell. By moving the end nodes of the spatial flexible struts to the corresponding substrate plates, each basic chiral unit is equivalent to an extended spatial beam element with two nodes, implying that the hierarchical chiral elementary cell can be described by three nodes. Upon modular assembly of the three basic chiral units, labelled ①, ②, and ③, the global dynamic stiffness matrix is obtained, with the assembly procedure analogous to the finite element method.

$$\begin{bmatrix} \mathbf{F}_{int}(\omega) \\ \mathbf{0} \end{bmatrix} = \begin{bmatrix} \mathbf{D}_{\mathrm{e}} & \mathbf{D}_{\mathrm{ef}} \\ \mathbf{D}_{\mathrm{ef}}^{\mathrm{T}} & \mathbf{D}_{\mathrm{f}} \end{bmatrix} \begin{bmatrix} \mathbf{X}_1 \\ \mathbf{X}_{\mathrm{f}} \end{bmatrix} \tag{10}$$

where the subscripts 'e' and 'f' correspond to the "essential'' and "free'' boundary conditions. As a result, the unknown quantities can be resolved as

$$\begin{cases} \mathbf{X}_{\mathrm{f}} = -\mathbf{D}_{\mathrm{f}}^{-1}\mathbf{D}_{\mathrm{ef}}^{\mathrm{T}}\mathbf{X}_1 \\ \mathbf{F}_{int} = (\mathbf{D}_{\mathrm{e}} - \mathbf{D}_{\mathrm{ef}}\mathbf{D}_{\mathrm{f}}^{-1}\mathbf{D}_{\mathrm{ef}}^{\mathrm{T}})\mathbf{X}_1 \end{cases} \tag{11}$$

From the analytical solution presented in Eq. (11), we can extract the vibration amplitudes at the input and output ports, which are denoted as x_i and x_o, respectively. According to the physical definition, the vibration transmittance through the hierarchical chiral mechanical metamaterial is computed as

$$\psi(\omega) = 20\log(x_o/x_i) \tag{12}$$

When the vibration at the output port is smaller than that at the input port, i.e., $\psi(\omega) < 0$, vibration suppression occurs, which is an essential condition for the band gap formation.

3.2. Band structure analysis for hierarchical chiral metamaterials

As a fundamental analytical tool in wave propagation, band structure [52,86] provides critical insights into dispersion relations and band gap identification. Consequently, this subsection is devoted to formulating their band structures to characterize the wave propagation properties within hierarchical chiral metamaterials.

To begin the formulation, a transfer matrix is constructed to link the nodal force and modal displacement at the input and output ports. For this purpose, all nodes within a representative volume element (RVE) are classified into three categories: the input node, the output node, and the intermediate nodes. The corresponding variables are denoted by the subscripts 'int', 'out', and 'mid', respectively. For an RVE comprising two hierarchical chiral elementary cells, its dynamic governing equation can be reconstructed as

$$\begin{bmatrix} \mathbf{F}_{int} \\ \mathbf{F}_{\mathrm{out}} \\ \mathbf{0}_{3\times 6} \end{bmatrix} = \begin{bmatrix} \mathbf{D}_{\mathrm{UL}} & \mathbf{D}_{\mathrm{UM}} & \mathbf{D}_{\mathrm{UR}} \\ \mathbf{D}_{\mathrm{ML}} & \mathbf{D}_{\mathrm{MM}} & \mathbf{D}_{\mathrm{MR}} \\ \mathbf{D}_{\mathrm{BL}} & \mathbf{D}_{\mathrm{BM}} & \mathbf{D}_{\mathrm{BR}} \end{bmatrix} \begin{bmatrix} \mathbf{X}_{int} \\ \mathbf{X}_{\mathrm{out}} \\ \mathbf{X}_{\mathrm{mid}} \end{bmatrix} \tag{13}$$

After eliminating the intermediate nodes, the following expression is obtained with the transfer matrix $\mathbf{T}_d$:

$$\begin{bmatrix} \mathbf{X}_{int} \\ \mathbf{F}_{int} \end{bmatrix} = \begin{bmatrix} -\mathbf{A}^{-1}\mathbf{B} & \mathbf{A}^{-1} \\ \mathbf{D} - \mathbf{C}\mathbf{A}^{-1}\mathbf{B} & \mathbf{C}\mathbf{A}^{-1} \end{bmatrix} \begin{bmatrix} \mathbf{X}_{\mathrm{out}} \\ \mathbf{F}_{\mathrm{out}} \end{bmatrix} = \mathbf{T}_d \begin{bmatrix} \mathbf{X}_{\mathrm{out}} \\ \mathbf{F}_{\mathrm{out}} \end{bmatrix} \tag{14}$$

where the associated block matrices are derived as

$$\begin{cases} \mathbf{A} = \mathbf{D}_{\mathrm{ML}} - \mathbf{D}_{\mathrm{MR}}\mathbf{D}_{\mathrm{BR}}^{-1}\mathbf{D}_{\mathrm{BL}} \\ \mathbf{B} = \mathbf{D}_{\mathrm{MM}} - \mathbf{D}_{\mathrm{MR}}\mathbf{D}_{\mathrm{BR}}^{-1}\mathbf{D}_{\mathrm{BM}} \\ \mathbf{C} = \mathbf{D}_{\mathrm{UL}} - \mathbf{D}_{\mathrm{UR}}\mathbf{D}_{\mathrm{BR}}^{-1}\mathbf{D}_{\mathrm{BL}} \\ \mathbf{D} = \mathbf{D}_{\mathrm{UM}} - \mathbf{D}_{\mathrm{UR}}\mathbf{D}_{\mathrm{BR}}^{-1}\mathbf{D}_{\mathrm{BM}} \end{cases} \tag{15}$$

On this basis, we further apply the Bloch-Floquet principle to obtain the dispersion relation of the periodic hierarchical chiral metamaterial, which takes the form:

$$\begin{bmatrix} \mathbf{X}_{\mathrm{out}} \\ \mathbf{F}_{\mathrm{out}} \end{bmatrix} = e^{iq(2h_c+4h_p)} \begin{bmatrix} \mathbf{I}_{6\times 6} & \mathbf{0}_{6\times 6} \\ \mathbf{0}_{6\times 6} & \mathbf{I}_{6\times 6} \end{bmatrix} \begin{bmatrix} \mathbf{X}_{int} \\ \mathbf{F}_{int} \end{bmatrix} \Leftrightarrow \begin{bmatrix} \mathbf{X}_{int} \\ \mathbf{F}_{int} \end{bmatrix} = e^{-iq(2h_c+4h_p)}\mathbf{I}_{12\times 12} \begin{bmatrix} \mathbf{X}_{\mathrm{out}} \\ \mathbf{F}_{\mathrm{out}} \end{bmatrix} \tag{16}$$

where q denotes the wavenumber, and $\mathrm{i} = \sqrt{-1}$ represents the imaginary unit. By comparing Eq. (14) with Eq. (16), we obtain a standard eigenvalue problem:

$$\left|\mathbf{T}_d - e^{-\mathrm{i}q\left(2h_s+4h_p\right)}\mathbf{I}_{12\times 12}\right| = 0 \tag{17}$$

For a specified angular frequency ω, the corresponding wavenumber q can be computed using Eq. (17). Through a systematic sweep of ω and subsequent plotting of the resultant q, the band structure of the chiral metamaterial is visualized, allowing for the thorough analysis of band gap features.

4. Experimental verification and simulation validation

In this section, the established theoretical formulation will be verified through a comprehensive comparison with both FE simulations and experimental measurements. To affirm the accuracy and reliability of the model, the transmittance spectra and band

structure of hierarchical chiral metamaterials with distinct elementary cells will be examined in detail.

4.1. Theoretical model validation

As depicted in Fig. 4, two representative hierarchical chiral metamaterials are analyzed in this verification case study. Both metamaterials comprise 8 elementary cells, arranged in a linear array along their longitudinal direction. The first configuration is formed by homogeneous RRR-LLL unit cells, while the second is constructed with mirrored-symmetric RLR-LLR unit cells. The specific dimensional parameters for these two hierarchical chiral metamaterials are outlined in Table 1. Unless otherwise specified, these parameters will be adopted as the default settings for all subsequent analyses.

According to the developed theoretical formulation, the global dynamic response, including vibration characteristics and band structures, is calculated using our in-house spectral element code. To assess its validity, the band gap properties of these two hierarchical chiral metamaterials subjected to harmonic excitation are simulated through an FE model, which is implemented in COMSOL Multiphysics® software. Additionally, for experimental validation of the vibration suppression performance, 3D printing technology is used to fabricate prototypes of the two metamaterials. The chosen Nylon material has a mass density of 1160 kg/m^3, an elastic modulus of 2.51 $\times$ 10^{9}N/m^2, and a Poisson's ratio of 0.41.

Fig. 4 depicts the overall experimental setup. The prototype is suspended with two mounting brackets to provide gravity compensation. The mechanical excitation at one end of the specimen is precisely generated and controlled using an electrodynamic shaker (Model 2060E) driven by a power amplifier (Modal Shop). The vibration transmissibility across the hierarchical chiral metamaterial is continuously monitored by two accelerometer sensors (YMC122A). These acquired signals are recorded through a data acquisition system (ECON MI-7008) and then transferred for post-processing analysis on a laptop computer.

In the proposed hierarchical chiral metamaterial featuring four RRR-LLL unit cells, the wave propagation of symmetric longitudinal modes exhibits two complete band gaps below 2000 Hz. As shown in the aqua-highlighted region of Fig. 5(a), these band gaps are located within the frequency ranges of 170.4–1002.1 Hz and 1505.7–1804.1 Hz, with the normalized bandwidth of the first band gap being 1.42. For the hierarchical chiral metamaterial featuring 4 RLR-LLR unit cells, two broader band gaps occur at lower frequencies. As shown in Fig. 5(b), the corresponding frequency ranges for these band gaps are 96.6–976.0 Hz and 1220.3–1755.1 Hz, with the normalized bandwidth of the initial band gap increasing to 1.64.

Fig. 5 also indicates that the predicted band gap intervals for the two metamaterials are in excellent agreement with both the COMSOL simulation results and experimental measurements. This great consistency confirms the reliability of the theoretical formulation for the vibration response analysis of hierarchical chiral metamaterials. In addition, the computational efficiency of this theoretical model is evident. Utilizing a desktop system with a 3.40 GHz processor, the MATLAB-based theoretical analysis is completed within 5.14 s. In comparison, the COMSOL simulation necessitates a much longer processing time, approximately 8.53 $\times$ 10^4 s. These results highlight the efficacy of the developed theoretical model for the transmittance spectra prediction of hierarchical chiral metamaterials.

Furthermore, the band structures are computed to confirm the band gap properties of the two metamaterials. Under the applied excitation condition, only symmetric longitudinal modes are triggered, which are depicted as red-colored branches in Fig. 6. Notably, the attenuation valleys between the red curves perfectly match the transmittance analysis results shown in Fig. 5. In addition, theoretical dispersion relation solutions, plotted by blue-point branches, align well with the COMSOL simulation results. As demonstrated in Fig. 6, the close agreement between theoretical predictions and simulation data further validates the accuracy of the derived formulation for band structure characterization.

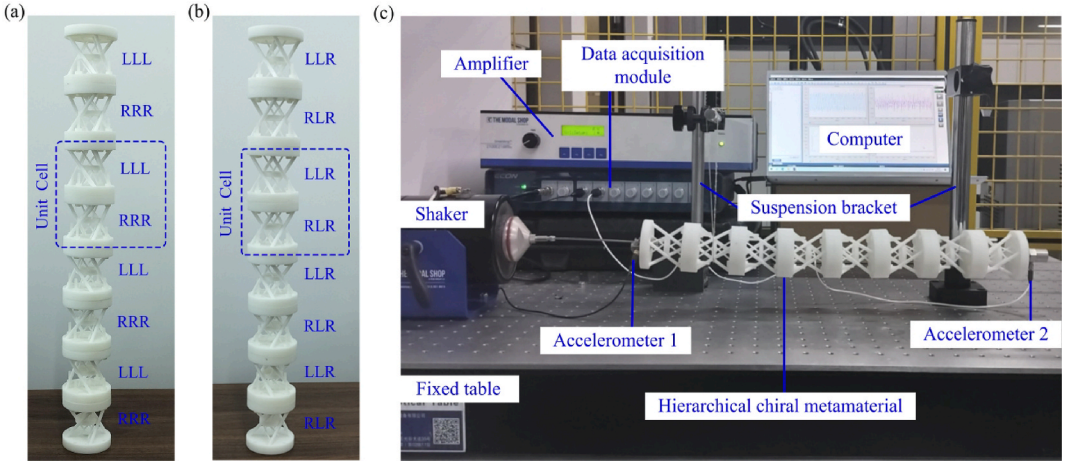

Fig. 4. Experimental test on the vibration suppression performance of hierarchical chiral metamaterials. (a) Prototype of the hierarchical chiral metamaterial with 4 RRR-LLL unit cells; (b) Prototype of hierarchical chiral metamaterial with 4 RLR-LLR unit cells. (c) Vibration transmittance response measurement.

Table 1
Dimensional parameters of the hierarchical chiral metamaterials (unit: mm).

Dimensional parameter	External chiral frame		Internal chiral unit	
	Symbol	Value	Symbol	Value
Length of inclined struts	l_c	53.15	l_a	23.05
Diameter of inclined struts	d_c	4.00	d_a	2.00
Height of substrate plates	h_p	10.00	h_m	5.00
Diameter of substrate plates	d_p	60.00	d_m	28.00
Height of chiral units	h_c	40.00	h_a	17.50

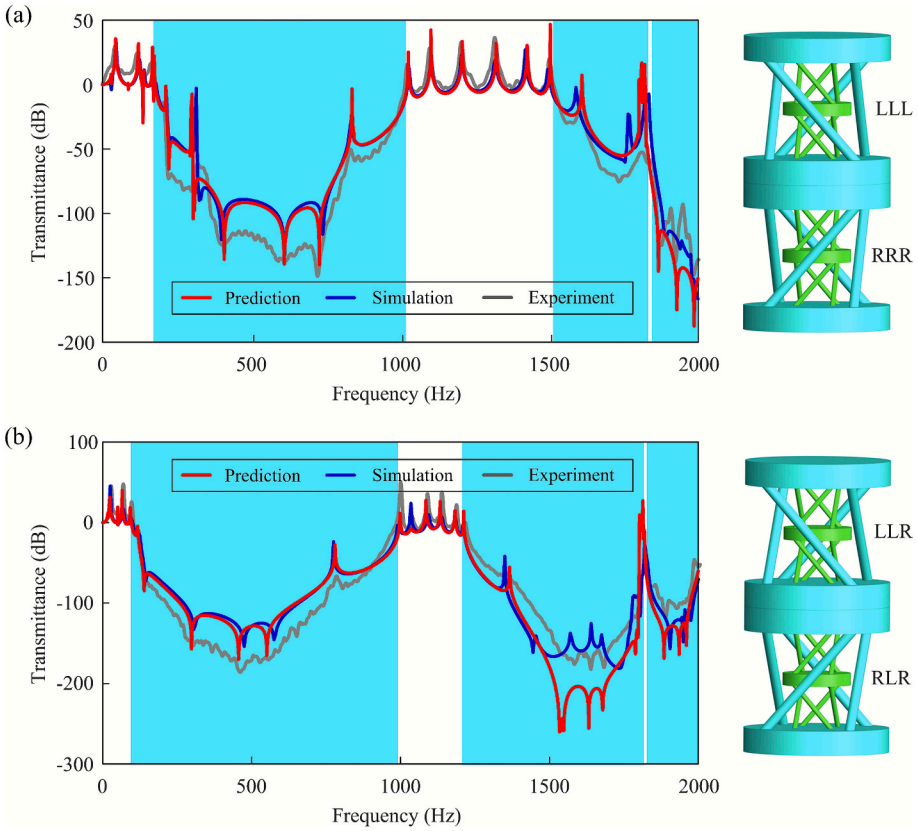

Fig. 5. Transmittance spectra comparison from theoretical predictions, simulational results, and experimental measurements. (a) Transmittance for the hierarchical chiral metamaterial with 4 RRR-LLL unit cells; (b) Transmittance for the hierarchical chiral metamaterial with 4 RLR-LLR unit cells.

4.2. Formation mechanism of band gaps

In this subsection, the eigenmodes at the band gap boundaries are examined to facilitate a deeper understanding of the wave propagation characteristics within the metamaterial. Through this thorough analysis, we elucidate the band gap formation mechanisms of such hierarchical chiral metamaterials.

Due to its semi-analytical nature, the SEM is highly efficient in computing vibration transmittance and band structures for such metamaterials, but it is not suitable to characterize the localized deformation fields. To remedy this, a FE model with a refined mesh of continuum elements is constructed in COMSOL Multiphysics® to capture the edge modes of the unit cell. Through the application of Floquet periodic boundary conditions and a parametric sweep, the specific mode shapes at relevant frequencies are determined, providing a clear insight into the underlying formation mechanisms of band gaps.

Fig. 7(a) presents the edge modes of the chiral metamaterial configured with RRR-LLL unit cells. As marked in Fig. 6(a), modes A and B define the lower and upper edges of the first band gap, while modes C and D bound the second. An examination of modes A and B in Fig. 7(a) shows that the two adjacent outer hierarchical substructures exhibit opposite chirality, i.e., right- and left-handed, respectively. The overall deformation of the entire structure is dominated by rotational motion. Mode B shows that the top and bottom discs rotate clockwise while the middle disc rotates counterclockwise. Because the upper and lower substructures have opposite chirality, the chiral ligaments transmit torques of opposite sign across the mid-plane. The resulting counter-rotation creates

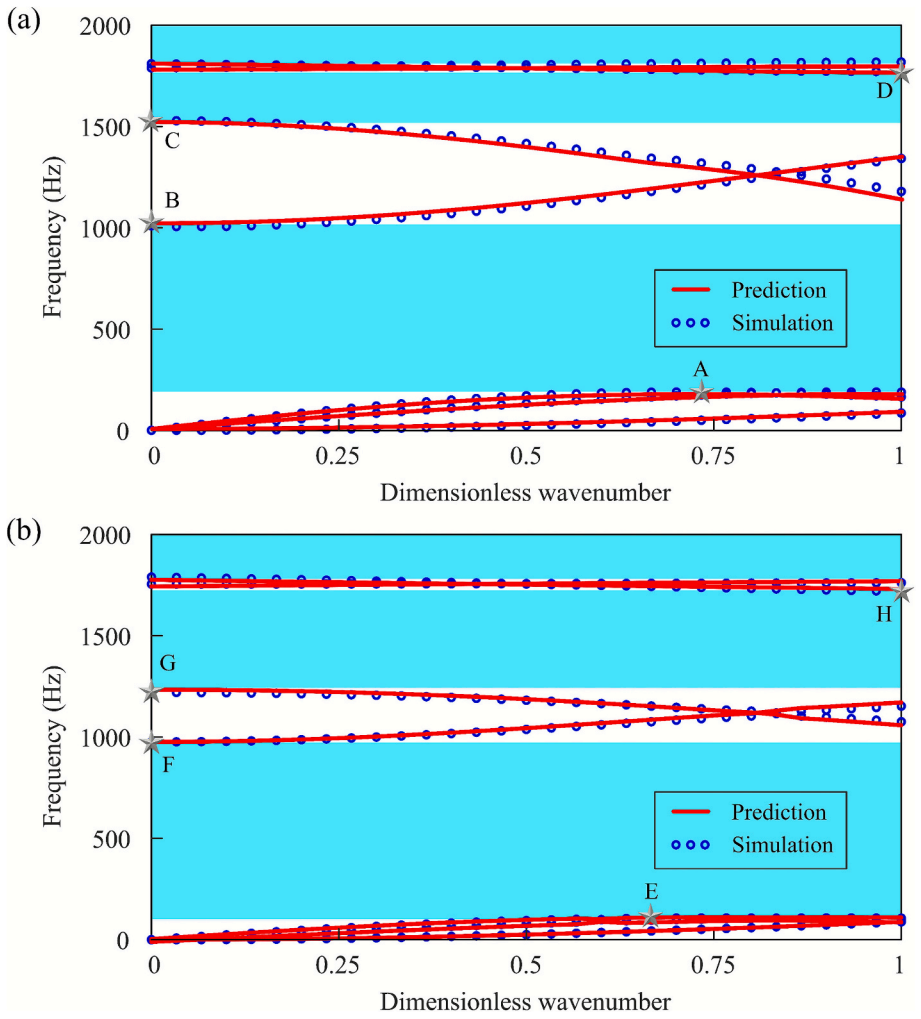

Fig. 6. Band structures of hierarchical chiral metamaterials for the symmetric longitudinal mode. (a) Dispersion relation for the metamaterial with RRR-LLL unit cells. (b) Dispersion relation for the metamaterial with RLR-LLR unit cells. The band gaps, highlighted in the aqua regions, exhibit good consistency with the band gaps extracted from the transmittance spectra.

an interlocking, gear-like motion that cancels the net twist/axial motion at the interfaces. Energy is thus confined in a localized rotational mode, the group velocity approaches zero, and the wave cannot propagate, opening the first band gap. In this RRR-LLL chiral metamaterial, the internal hierarchical substructures adopt the same chiral arrangement as the external ones. As a result, their vibration modes closely mirror those of the outer substructures.

Inspection of modes C and D in Fig. 7(a) reveals a distinct formation mechanism for the second band gap. The deformation localizes within the internal hierarchical substructures, which play the role of embedded resonators. In the lower-edge mode C, the internal discs exhibit a pronounced torsional resonance while the outer frame remains nearly still, indicating energy trapping inside the internal hierarchical substructures. Moreover, the internal resonators rotate out of phase with the surrounding lattice, leading to torque cancellation and minimal power flow across the interfaces. These features indicate that the second gap is produced by the coupling between lattice waves and the torsional resonance of the internal substructures.

Similarly, Fig. 7(b) presents the edge modes of the chiral metamaterial configured with RLR-LLR unit cells. As correspondingly indicated in Fig. 6(b), modes E and F delineate the lower and upper edges of the first band gap of this RLR-LLR chiral metamaterial, while modes G and H bound the second one. Though the internal hierarchical substructures in this RLR-LLR metamaterial are arranged in different chirality, modes E and F resemble modes A and B. Deformation localizes in the outer hierarchical substructures. Moreover, as in mode B, mode F features clockwise rotation of the top and bottom discs and counterclockwise rotation of the middle disc. Therefore, one knows that the opening mechanism of the first band gap of the RLR-LLR chiral metamaterial is similar to that of the RRR-LLL metamaterial and primarily arises from counter-rotation-induced interlocking between adjacent outer hierarchical substructures. This is supported by the first band gaps of the two chiral metamaterials having similar widths and occurring over comparable frequency ranges. Importantly, the formation of the first band gap is not entirely independent of the internal hierarchy. Variations in internal chirality cause a slight change in the lower-edge frequency between the two chiral metamaterials, as can be

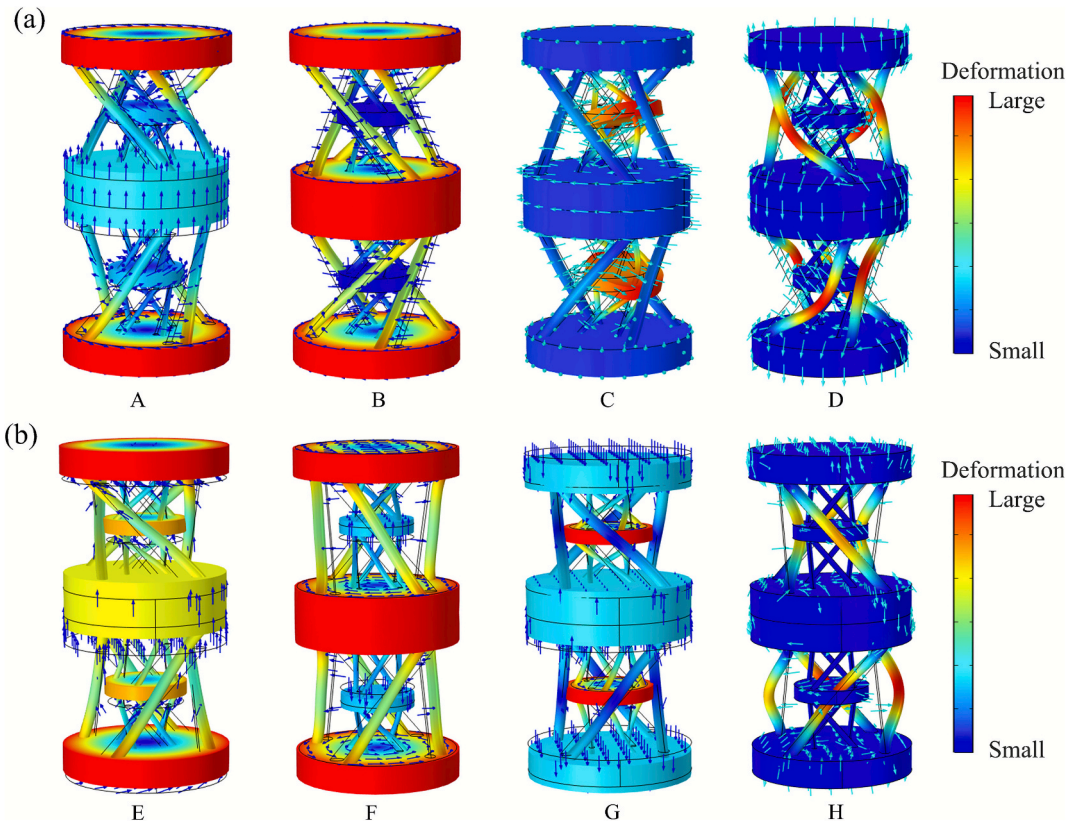

Fig. 7. Eigenmodes of the hierarchical chiral metamaterials at the band gap boundaries. (a) Eigenmodes of the RRR-LLL metamaterial. (b) Eigenmodes of the RLR-LLR metamaterial. For each panel, the two subplots on the left display the edge modes for the first band gap, while the two subplots on the right display the edge modes for the second band gap. The subscripts A-H correspond to specific edge locations, as indicated in Fig. 5.

observed in Fig. 5 and Fig. 6.

However, around the edges of the second band gap, modes G and H of the RLR-LLR chiral metamaterial are noticeably different from modes C and D of the RRR-LLL chiral metamaterial. In the lower-edge mode G, energy is confined to the internal hierarchical substructures, which undergo predominantly translational motion with no appreciable torsional resonance. Compared with mode C, mode G is nearly purely translational. This promotes a robust opening of the second band gap in the RLR-LLR chiral metamaterial, as evidenced by its substantially greater width and a markedly lower lower-edge frequency than in the RRR-LLL counterpart.

5. Vibration suppression performance of hierarchical chiral metamaterials

5.1. *Comparison of hierarchical and non-hierarchical metamaterials*

To examine the effectiveness of the hierarchical design strategy, this subsection will conduct a comprehensive comparison among three chiral metamaterials, i.e., the non-hierarchical syndiotactic chiral metamaterial (NSCM), the mono-hierarchical syndiotactic chiral metamaterial (MSCM), and the full-hierarchical syndiotactic chiral metamaterial (FSCM).

As illustrated in Fig. 8(a), the NSCM is a classic design known for opening broad and deep-subwavelength band gaps. Attributed to the inertial amplification and Thomson scattering effects, the NSCM weakens the link between the mass and inertia, enabling vibration suppression at lower frequencies with superior specific stiffness. Particularly, compared with the isotactic arrangement, the syndiotactic arrangement can further decrease the start frequency of the first band gap. Therefore, the NSCM is adopted as a strong reference for comparison. Fig. 8(b) depicts the unit cell of MSCM, where each layer includes a basic chiral unit serving as the local resonator, but the internal chiral structure is only unidirectional rather than bidirectional coupling with the external frame. As shown in Fig. 8(c), the HSCM corresponds to the hierarchical chiral metamaterial proposed in this study. The three types of syndiotactic chiral metamaterials have the same lattice constant. Besides, the external chiral frame of both MSCM and HSCM is identical to that of the NSCM.

To ensure the objectivity of the comparison, the normalized frequency f_n is introduced to eliminate the influence of structural stiffness and mass, which is expressed as

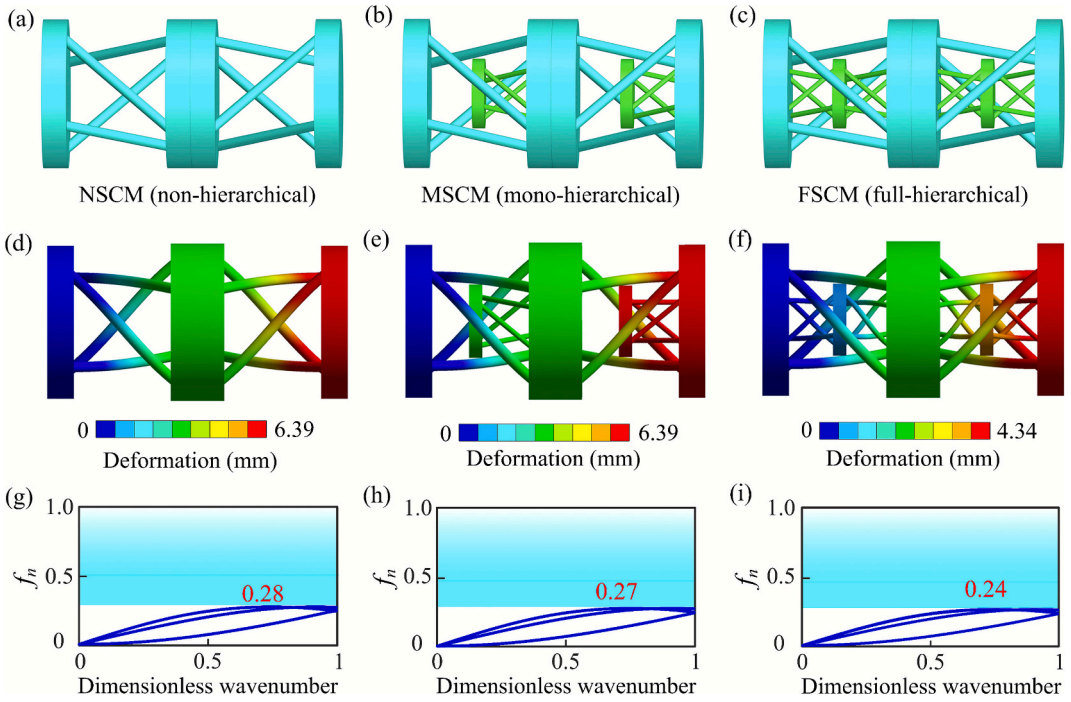

Fig. 8. Comparison of hierarchical and non-hierarchical syndiotactic chiral metamaterials. (a) The unit cell of non-hierarchical syndiotactic chiral metamaterial (NSCM); (b) The unit cell of mono-hierarchical syndiotactic chiral metamaterial (MSCM); (c) The unit cell of full-hierarchical syndiotactic chiral metamaterial (FSCM). Subplots (d), (e), and (f) depict the compression deformation of the unit cells for NSCM, MSCM, and FSCM, respectively, with a compression force of 100 N applied to the substrate plate. The dispersion spectra of the three chiral metamaterials are shown in subplots (g), (h), and (i), with the shaded regions indicating their first band gaps. The normalized starting frequencies are highlighted in red.

$$f_n = \frac{a}{v_0} f = \frac{f}{\sqrt{k_{\text{eff}}/m}} \tag{18}$$

Here, f represents the angular frequency, a is the lattice constant, and v_0 is the propagation speed of the longitudinal wave; k_{eff} and m are the effective compression stiffness and total mass of the unit cell, respectively.

By applying a compression force to the upper substrate plate, the deformation behavior of unit cells can be readily captured using finite element simulations. From the data in Fig. 8, the compression stiffness of the NSCM and MSCM is calculated to be 15.65 N/mm, while the HSCM exhibits a significantly higher value of 23.04 N/mm. The corresponding unit cell masses for the three metamaterials are 137.39 g, 145.21 g, and 145.88 g, respectively. Thus, the specific stiffness, defined as the ratio of stiffness to mass, for the NSCM is 0.1139, while the developed HSCM provides a better specific stiffness of 0.1579. This implies that the NSCM can withstand 1.38 times the load of the MSCM under the equivalent structural mass. Furthermore, as illustrated in Fig. 8(g)–(i), the normalized starting frequencies of the first band gap for the three metamaterials are 0.28, 0.27, and 0.24, respectively. Notably, the proposed HSCM has the lowest start frequency, decreasing it by 14.28 % compared to NSCM. These results demonstrate that the HSCM outperforms traditional syndiotactic chiral metamaterials for low-frequency vibration suppression, highlighting the advantages of the proposed hierarchical design strategy.

Beyond comparing hierarchical versus non-hierarchical configurations, we further discuss the effects of substituting embedded chiral struts with straight ones on the band gap properties. For brevity, we introduce the symbol “S” to represent the straight lattice configuration, aligning with the established abbreviations. As shown in Fig. 9, three distinct unit cells (RS-LS, RSS-LSS, and RSR-LLS) are constructed for syndiotactic chiral metamaterials, which are compared to the RLR-LLR configuration (shown in the right part of Fig. 8). Specifically, the RS-LS unit cell employs four straight struts as internal components, while the RSS-LSS and RSR-LLS unit cells replace one or two internal chiral lattices with straight struts. For comparison, the mass of each unit cell is matched to the RLR-LLR design by adjusting the straight strut diameters.

As demonstrated in Fig. 9, the RS-LS unit cell achieves the highest stiffness-to-mass ratio, surpassing the RSS-LSS and RSR-LLS configurations. Regarding band gap properties, the normalized starting frequencies for their initial band gaps are 0.25, 0.26, and 0.26, respectively, all of which occur at higher frequencies than the RLR-LLR configuration. While the normalized starting frequency of the RS-LS metamaterial is comparable to that of the RLR-LLR configuration, it exhibits the narrowest initial band gap compared to the other configurations depicted in Figs. 8 and 9. This systematic investigation confirms that the integrated chiral hierarchy of the RLR-LLR design is beneficial for generating the targeted low-frequency and wide band gaps. In contrast, when the chiral metamaterial is partially or fully de-chiralized, the vibration attenuation performance is markedly weakened.

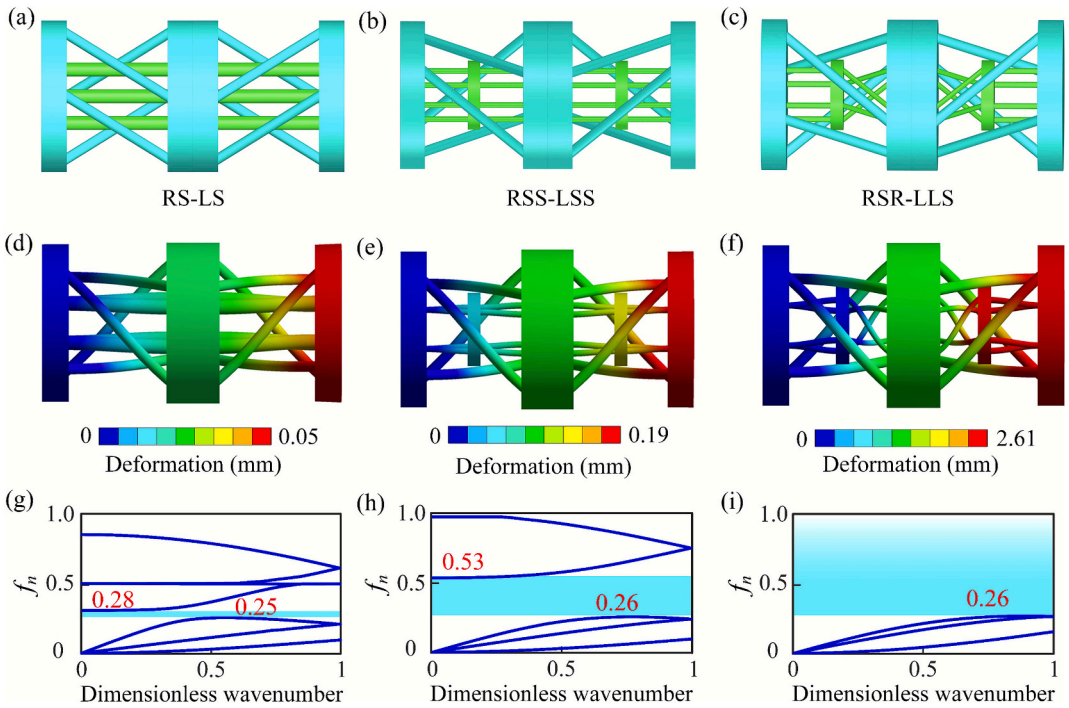

Fig. 9. Comparison of syndiotactic chiral metamaterials with embedded components involving straight struts. (a) The unit cell RS-LS, where "S" represents the straight strut; (b) The unit cell RSS-LSS; (c) The unit cell RSR-LLS. All unit cells have identical mass, achieved by adjusting the diameters of the straight struts. Subplots (d), (e), and (f) illustrate the compression deformation of the respective unit cells (RS-LS, RSS-LSS, RSR-LLS) under a 100 N compressive force applied to the substrate. The dispersion spectra for these three chiral metamaterials are shown in subplots (g), (h), and (i), with the shaded regions indicating the first band gaps.

5.2. *Parametric analysis for the band gap tailoring*

To elucidate the effects of critical geometric parameters on vibration suppression, this subsection performs a systematic parametric analysis for the hierarchical chiral metamaterials with eight elementary units, shedding light on the customization design of their band gaps.

Based on the design parameters for the hierarchical chiral metamaterials, the external strut diameter d_c is varied in the range of 2–6 mm to deduce their influence on transmittance spectra, while the internal strut diameter d_a is varied from 1 to 3 mm. As shown in Fig. 10(a), increasing d_c enlarges the first band gap but elevates its start frequency. In contrast, the second band gap shrinks with improved start frequency. Especially, the hierarchical chiral metamaterial with $d_c = 6$ mm yields an exceptionally wide band gap spanning over 212.7–1404.5 Hz. The corresponding normalized bandwidth is up to 1.47, which outperforms those reported in recent studies. In addition, Fig. 10(b) reveals that the internal strut diameter d_a predominantly modulates the start frequency of the second band gap for such hierarchical chiral metamaterials.

To investigate the characteristics of the band gap with different tilt angles, we calculated the transmission spectra for the three cases as shown in Fig. 10(c) and Fig. 10(d). Given the fixed lattice constant, the bigger the tilt angle, the shorter the strut length. The negative correlation means that the effects of tilt angle on the band gaps are also inverse to those of strut length. As depicted in Fig. 10 (c), increasing the external tilt angle θ_c reduces the cutoff frequency of the first band gap, simultaneously triggering the second band gap to move into the high frequency. Regarding the internal tilt angle θ_m, Fig. 10(d) indicates that its increase can shift the second band gap into low frequency, with negligible influence on the first band gap.

Since the mass of substrate plates is associated with the inertial amplification effect of such chiral metamaterials, the diameters of both external and internal substrate plates are also changed within the parametric analysis. As demonstrated in Fig. 10(e), larger external plates narrow the first band gap by decreasing its cutoff frequency and broaden the second band gap by decreasing the corresponding start frequency. For the diameter of the internal substrate plates, Fig. 10(f) implies that larger internal plates negatively correlate with the start frequency of the second band gap.

To summarize, although diverse structural parameters exert varying influences on the vibration suppression performance of the developed hierarchical chiral metamaterials, the parametric study reveals that the geometric parameters of the external frame mainly govern the first band gap, while those of the internal microstructure predominantly control the second band gap. In particular, the external strut diameter exerts significant concurrent influences on the properties of both the first and second band gaps for such metamaterials.

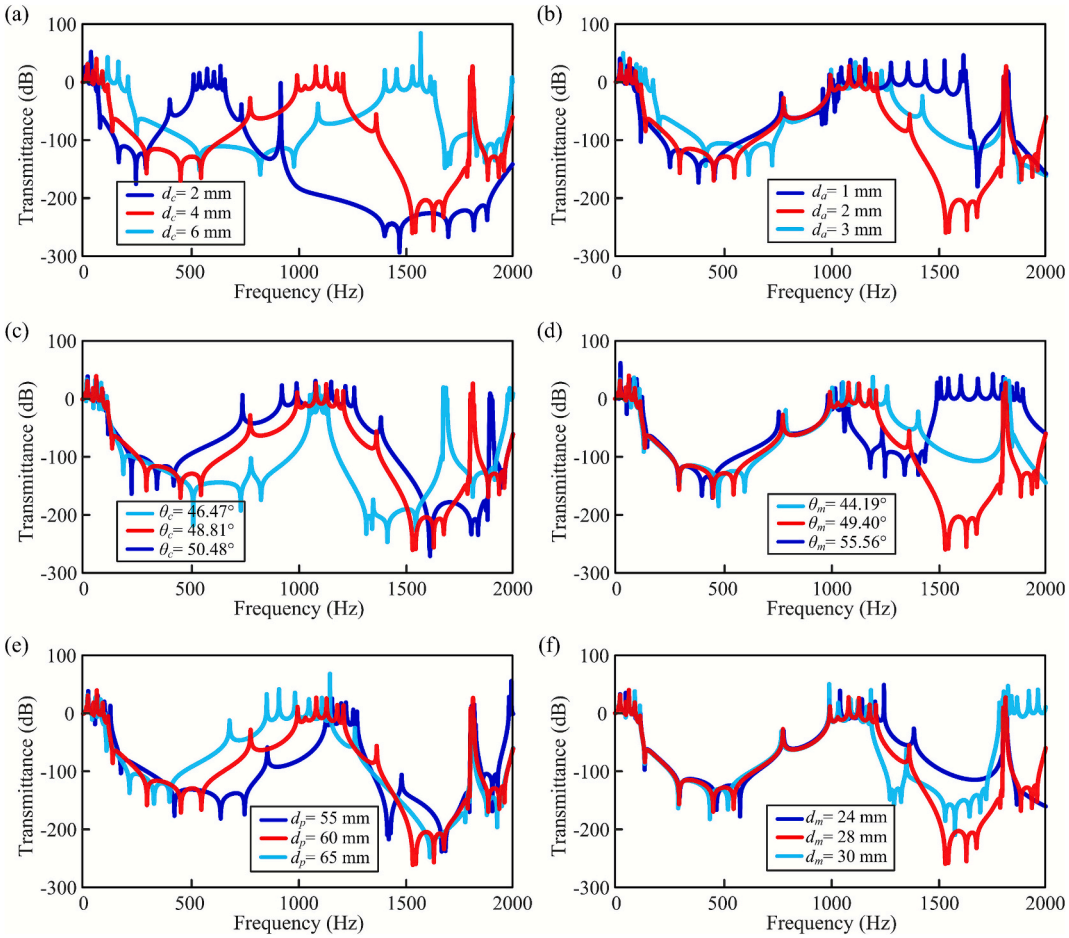

Fig. 10. Effects of independent geometric parameters on vibration suppression performance. (a) Effect of the diameters of external struts; (b) Effect of the diameters of internal struts; (c) Effect of the tilt angle of external struts; (d) Effect of the tilt angle of internal struts; (e) Effect of the diameter of the external substrate plates; (f) Effect of the diameter of the internal substrate plates.

5.3. Logic gate operations shaped by altering boundary conditions

Akin to the switching mechanism in electronic circuits, the proposed hierarchical chiral metamaterials can also achieve the basic logic gate operations by opening and closing the band gap at a specific frequency. This subsection will detail how the logic gate functionalities are shaped by alterations in the boundary conditions.

As illustrated in Fig. 11, two distinct constraint types are applied to the external substrate plates, serving as control signals. Specifically, the "1" status corresponds to imposing rotational constraints, while the "0" status refers to an unconstrained condition. By manipulating elastic waves under varying boundary conditions, such hierarchical chiral metamaterials can be programmed to open or close the band gap within a specific frequency range. In this context, the output transmittance greater than 0 dB is interpreted as "1", while a transmittance lower than or equal to 0 dB is regarded as "0".

The transmission profiles in Fig. 11 reveal whether or not imposing rotational constraints on the unit cells significantly influences the band gap properties of the metamaterials. For the hierarchical chiral metamaterial with the RLR-LLR unit cells, the AND, OR, NOR, and GND logic gates are realized across frequencies of 117–689 Hz, 696–904 Hz, 1802–1815 Hz, and 1352–1794 Hz, respectively. As shown in Fig. 11(d), the transmittance spectra of the hierarchical chiral metamaterial with the RLR-LLL unit cells exhibit the operation of AND, OR, and GND logic gates over the frequency ranges of 196–684 Hz, 742–900 Hz, and 1539–1818 Hz, respectively.

These observations confirm that the hierarchical chiral metamaterials are capable of executing certain fundamental logic operations, which have potential applications in identifying the ranges of vibration frequency and mechanical programming.

6. Hierarchical chiral metamaterials with periodicity or aperiodicity

In the literature, metamaterials are commonly studied in their periodic form. Nonetheless, integrating disorder into their design has the potential to greatly improve their performance, surpassing that of their periodic counterparts. In particular, the various

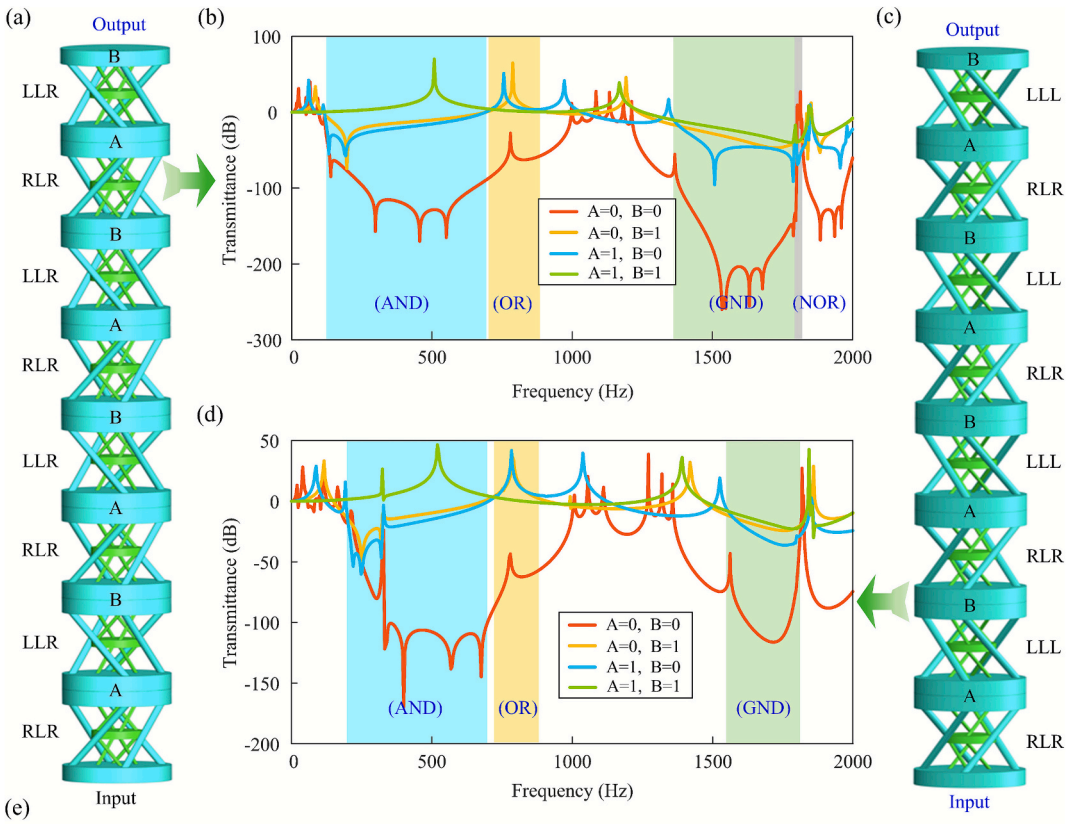

(e)

Logic gate	AND			OR			NOR			GND		
Truth table	A	B	Output	A	B	Output	A	B	Output	A	B	Output
	0	0	0	0	0	0	0	0	1	0	0	0
	0	1	0	0	1	1	0	1	0	0	1	0
	1	0	0	1	0	1	1	0	0	1	0	0
	1	1	1	1	1	1	1	1	0	1	1	0

Fig. 11. Logic gate functionalities of hierarchical chiral metamaterials under different boundary conditions. (a) Schematic diagram of the boundary constraint conditions for the hierarchical chiral metamaterial with RLR-LLR unit cells; (b) Transmittance spectra of the RLR-LLR metamaterial featuring the AND, OR, NOR, and GND logic gates; (c) Illustration of the boundary constraint conditions for the hierarchical chiral metamaterial with RLR-LLL unit cells; (d) Transmittance spectra of the RLR-LLL metamaterial exhibiting the operation of AND, OR, and GND logic gates; (e) Truth tables corresponding to the four primary logic gates.

configurations of hierarchical chiral metamaterials offer a broad spectrum of possibilities for manipulating wave propagation across a wide frequency range. This section will delve deeper into the superiority of aperiodic hierarchical chiral metamaterials in vibration suppression.

6.1. Band gap enhancement observed in aperiodic metamaterials

For such hierarchical chiral metamaterials, there are diverse combinations among 8 elementary cells that exhibit geometric similarity but dynamic disparity. Driven by these fascinating features, this subsection explores how different sequence variations affect vibration suppression, thus highlighting the application potential of aperiodic hierarchical chiral metamaterials.

Fig. 12 displays the mechanical and transmittance characteristics for the eight elementary cells. Despite possessing identical mass and external frame chirality, these elementary cells exhibit different loading capacity and transmittance patterns. The maximum support stiffness is observed for the configuration with identical internal chirality and opposing external chirality (e.g., RLL), while the minimum is found for internal alternating chirality. The case of fully identical chirality falls between these two extremes. In particular, enantiomeric pairs (e.g., RRL/LLR and RLR/LRL), featuring reversed chirality in both the external frame and internal microstructure, possess identical support stiffness and transmittance spectra.

However, uniform chirality in isotactic arrangements triggers torsion accumulation along the longitudinal direction, shaping a macroscopic tension–torsion coupling effect. In contrast, the alternating left-/right-handed chirality in syndiotactic arrangements

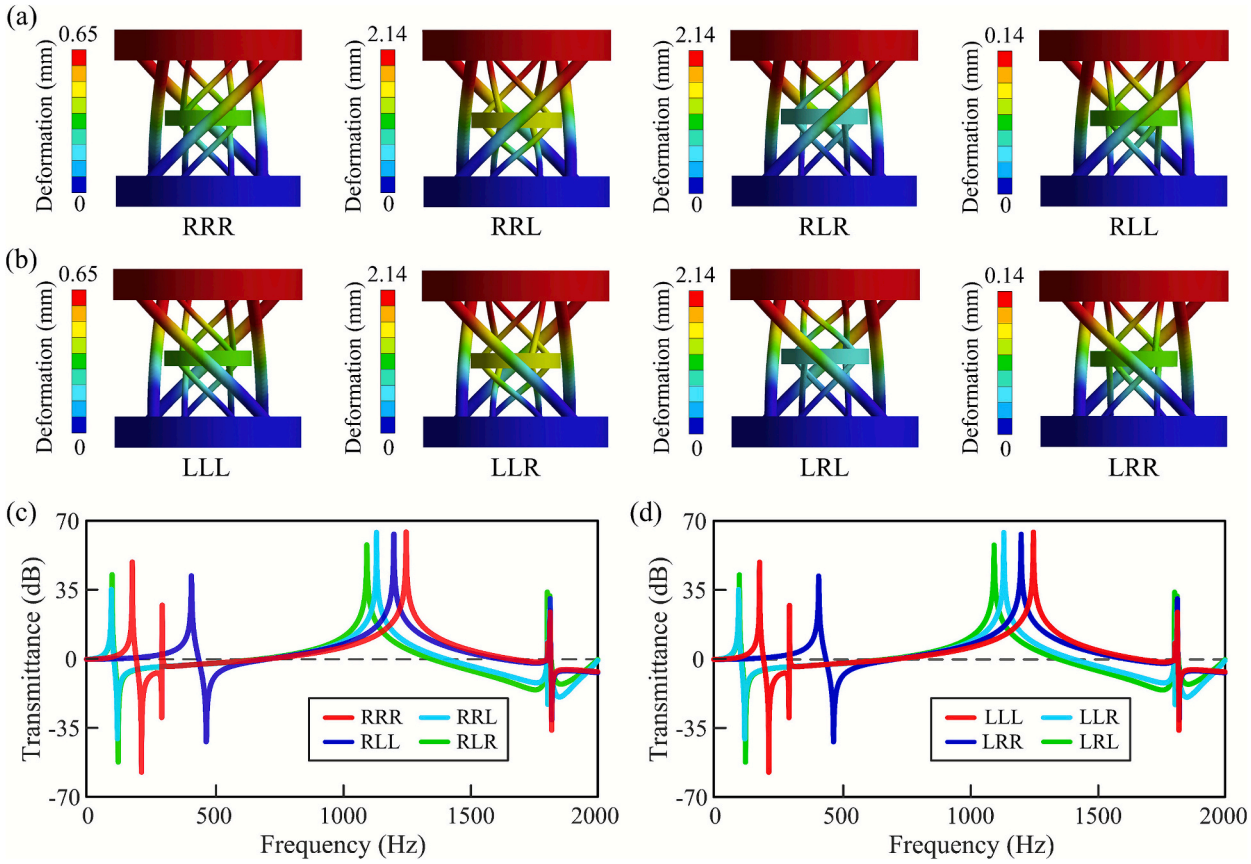

Fig. 12. Mechanical and transmittance characteristics of elementary cells for the hierarchical chiral metamaterials. (a) and (b) depict the compression deformation of four elementary cells with the left/right-chiral external frame, respectively. The lower substrate plate is fixed, while the upper substrate plate is subjected to a compression force of 100 N. (c) and (d) display the transmittance of four elementary cells with the left/right-chiral external frame, respectively.

produces opposing rotations that counteract torsion. The phase cancellation results in scattered waves of the same vibrational mode oscillating in opposed directions within syndiotactic chiral systems. Therefore, although each elementary cell can find a symmetric configuration with the same transmittance characteristics, the enantiomeric pairs exhibit the wave propagation performance when they are put into aperiodic hierarchical chiral metamaterials.

These observations naturally lead to the question: Can band gap enhancement be achieved by hybridizing dissimilar elementary cells? More precisely, does the deliberate disruption of structural symmetry contribute to broadening the band gap width or reducing the band gap start frequency?

To elucidate the significant impact of both internal chirality and external chirality on vibration suppression, as depicted in Fig. 13 (a), we compare hierarchical chiral structures that share a similar overall structure but feature different elementary cells. Based on the developed vibration response prediction model, the transmittance spectra are computed as presented in Fig. 13(b) and (c). By definition, the band gap occurs when $\psi(\omega) < 0$. Therefore, the corresponding starting and cutoff frequencies can be identified by examining the boundaries of the positive–negative transition. For the aperiodic hierarchical chiral structures analyzed, their initial band gaps span the ranges 82.4–1055.8 Hz, 91.1–1048.7 Hz, 69.5–1034.2 Hz, and 71.9–1045.2 Hz, respectively. For reference, the period metamaterial with an RLR-LLR unit cell has an initial band gap ranging from 96.6 Hz to 976.0 Hz. Notably, all four aperiodic configurations exhibit a broader first band gap. Furthermore, the last two configurations display a significantly reduced start frequency. Specifically, the expansion of the bandwidth is up to 10.68 %, while the start frequency is decreased by 28.05 %.

It is noteworthy that not all aperiodic designs contribute to the enhancement of vibration suppression. As observed in Fig. 14, the two illustrative aperiodic configurations actually exhibit a narrower band gap width compared to the periodic metamaterial with an RLR-LLR unit cell. This performance degradation stems from non-optimized unit arrangements, which disrupt wave propagation and fragment the band gap. Therefore, random unit combinations, without meticulous design, generally interfere with low-frequency elastic waves, leading to diminished attenuation region and contracted band width.

As demonstrated above, it is evident that aperiodic metamaterials have the potential to enhance the vibration suppression performance with a lower start frequency and wider bandwidth simultaneously. This finding underscores how strict periodicity inherently constrains the performance of mechanical metamaterials, while meticulous aperiodic design can unlock superior functionalities in the

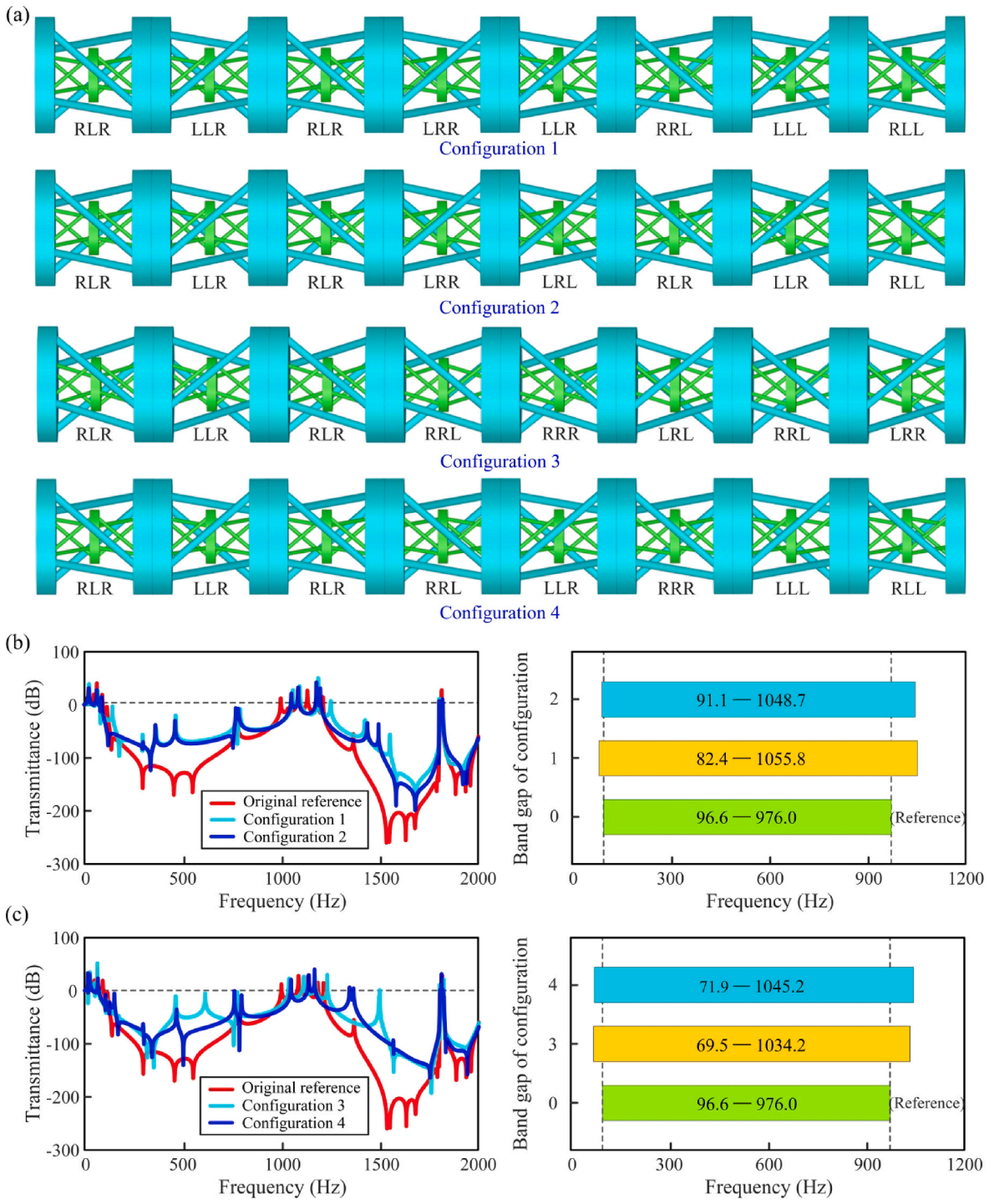

Fig. 13. Band gap enhancement observed in aperiodic metamaterials. (a) Four distinct aperiodic configurations, each composed of eight elementary cells. (b) Transmittance spectra of the first two aperiodic configurations, where the initial band gaps span 82.4–1055.8 Hz and 91.1–1048.7 Hz, respectively. (c) Transmittance spectra of the last two aperiodic configurations, with their first band gaps covering the frequencies of 69.5–1034.2 Hz and 71.9–1045.2 Hz, respectively. When compared to the period RLR-LLR metamaterial with its initial band gap spanning 96.6–976.0 Hz, the four aperiodic configurations exhibit a broader first band gap. Moreover, the last two configurations feature a lower start frequency.

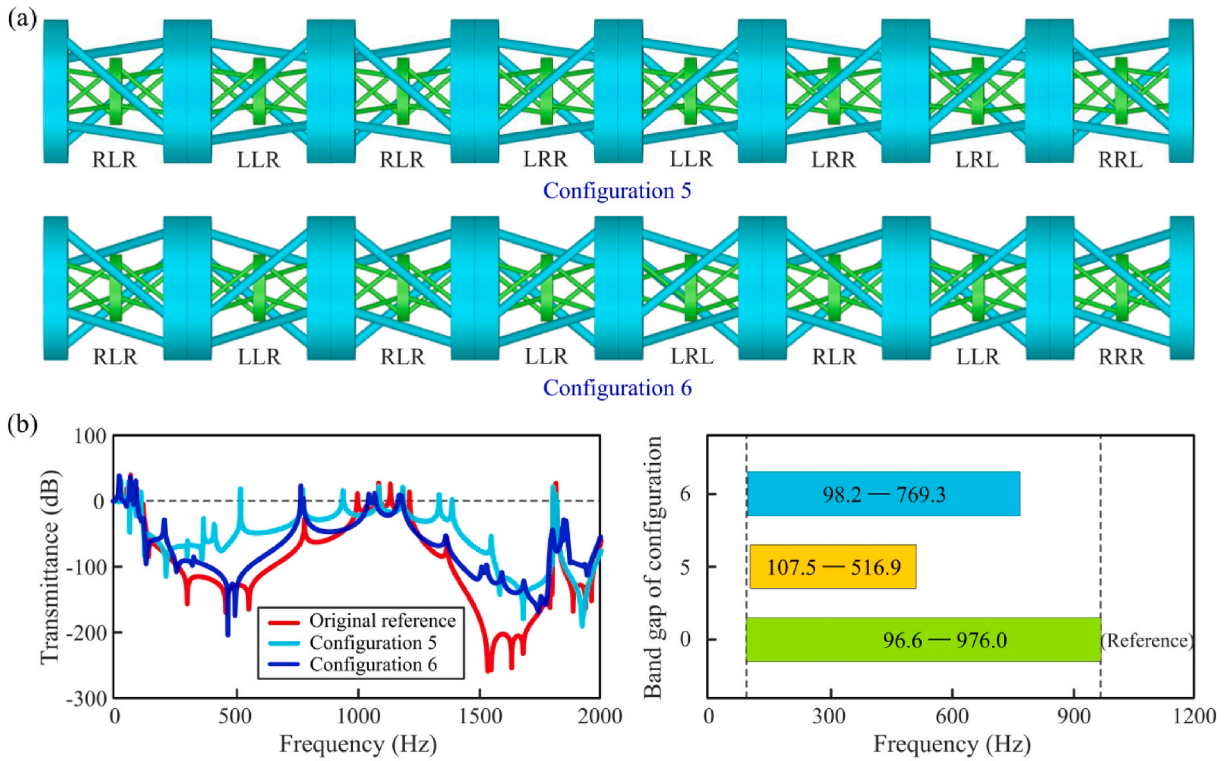

Fig. 14. Deterioration of the band gap width in aperiodic metamaterials. (a) Schematic representation of two different aperiodic configurations, each containing eight elementary cells. (b) The transmittance spectra for these configurations show initial band gaps of 98.2–769.3 Hz and 107.5–516.9 Hz, respectively. Compared to the periodic metamaterial with an RLR-LLR unit cell, both aperiodic configurations exhibit a narrower first band gap.

developed hierarchical chiral metamaterials.

6.2. *Widening band gap via parameter optimization design*

From the perspective of geometrical design, the aperiodicity of metamaterials exists in distinct topological configurations and nonuniform structural parameters. Having confirmed the effects of aperiodic configuration on the vibration suppression performance, we will further discuss the benefits of parameter optimization for the customization design of band gaps in this subsection.

Note that the minimum start frequency and the maximum width of the band gap are effective metrics assessing the vibration suppression capability of mechanical metamaterials. In this context, as commonly adopted in previous studies [51,87], the optimization target is set to widen the band gap interval while maintaining the overall structural dimension and the designated center frequency. As indicated in Fig. 10, the diameter d_c is more sensitive than the other geometric parameters to the band gap variations, and thus we choose it as a representative optimization variable. For description, the radius of external struts for the i-th elementary cell is detailed as $d_{c,\,i}$. Considering the structural manufacturability and spatial interference, the radius $d_{c,\,i}$ is limited to the range from 1 mm to 6 mm. Moreover, for comprehensively releasing the potential of the aperiodic metamaterials, the topological configuration is also incorporated into the band gap customization design. Herein, the binary coding scheme is employed for the topological sequence $[e_{c,\,i},\, b_{c,\,i},\, t_{c,\,i}]$ to characterize the left- and right-chiral elementary units. Specifically, $e_{c,\,i}$ denotes the chirality of the external frame, while $b_{c,\,i}$ and $t_{c,\,i}$ denote the chirality of the bottom and top internal macrostructure, respectively.

As presented above, the band gap optimization model for the developed hierarchical chiral metamaterials with eight elementary cells is summarized as follows:

$$\begin{cases} \text{find} \quad \boldsymbol{x} = [d_{c,1}, e_{c,1}, b_{c,1}, t_{c,1}, \cdots, d_{c,8}, e_{c,8}, b_{c,8}, t_{c,8}] \\ \quad \max \quad f(\boldsymbol{x}) = 2(f_{\text{end}} - f_{\text{start}})/(f_{\text{start}} + f_{\text{end}}) \\ \qquad s.t. \qquad f_{\text{start}} < f_{\text{target}} < f_{\text{end}} \\ \qquad 1 \leqslant \quad d_{c,i} < 6 \qquad (i = 1, 2, \cdots, 8) \\ \qquad e_{c,i} = 0 \quad \text{or} \quad 1 \qquad (i = 1, 2, \cdots, 8) \\ \qquad b_{c,i} = 0 \quad \text{or} \quad 1 \qquad (i = 1, 2, \cdots, 8) \\ \qquad t_{c,i} = 0 \quad \text{or} \quad 1 \qquad (i = 1, 2, \cdots, 8) \end{cases} \tag{19}$$

where f_{start}, f_{end}, and f_{target} correspond to the start frequency, end frequency, and target frequency of the first band gap, respectively.

Since this formulation involves both the continuous and discrete design parameters, the mixed-variable particle swarm optimization algorithm [88] is adopted to solve the optimization problem.

Taking the period metamaterial with four RLR-LLR unit cells as a reference, the target center frequency is set as 600 Hz. In the particle swarm algorithm, the population size is 50, and the maximum iteration number is 200. From the optimization process as provided in Fig. 15 (a), it can be seen that the bandwidth reaches the maximum after 138 iterations. The corresponding optimization result is listed in Fig. 15(b). Notably, aperiodicity exists in the chirality of both the external frames and the internal microstructures. The diameter distribution of the external frames is also non-uniform and non-gradient. Fig. 15(c) depicts the transmittance spectrum of the aperiod metamaterial after optimization, whose first vibration suppression zone spans 63.4–2017.3 Hz. This corresponds to a normalized bandwidth exceeding 1.87, signifying the attainment of broadband vibration suppression. Compared to the periodic reference configuration, the aperiodic design not only broadens the initial band gap by 122.2 % but also reduces the starting frequency by 34.4 %.

To further examine the effectiveness of the vibration suppression, the three representative vibration modes at 300 Hz, 600 Hz, and 1200 Hz are provided in Fig. 15(d). For the three vibration modes, it can be observed that peak vibrational amplitudes are concentrated in the initial two elementary cells, while the vibration displacement at the output end is significantly smaller than that of the input end, indicating the excellent vibration suppression performance.

As demonstrated above, it can be concluded that the hierarchical chiral metamaterials with twofold aperiodicity have more advantages over the periodic configurations in widening band gaps. In particular, without resorting to the respective parametric modeling and simulation software, the developed theoretical model paves the way to the on-demand band gap customization for such aperiodic hierarchical chiral metamaterials. Furthermore, the generality of the developed optimization framework allows its extension to the design of broader aperiodic mechanical metamaterials, supporting the exploration of diverse vibration suppression properties of interest.

Since this study focuses on low-frequency broadband vibration attenuation, the bandwidth and starting frequency are adopted as key performance metrics. Nonetheless, the developed framework supports the customization of the optimization objective to meet specific design requirements. For example, if a trade-off between attenuation amplitude and bandwidth is desired for the hierarchical chiral metamaterial, the corresponding objective function can be defined as:

$$\max \quad f(\boldsymbol{x}) = w_1 (f_{\text{end}} - f_{\text{start}})/(f_{\text{start}} + f_{\text{end}}) + w_2 \left\| \psi_{\min}/\psi_{\text{ref}} \right\| \tag{20}$$

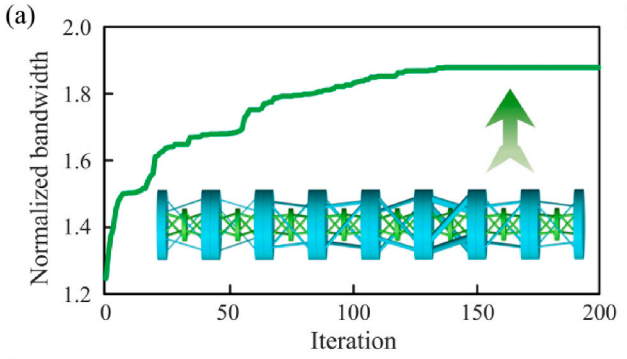

(b)

i	$d_{c,i}$ (mm)	$e_{c,i}$	$b_{c,i}$	$t_{c,i}$
1	1.14	1	0	1
2	1.02	0	1	0
3	1.99	1	0	1
4	3.07	0	0	1
5	3.45	1	1	1
6	5.98	0	1	0
7	2.37	0	0	1
8	1.35	1	1	0

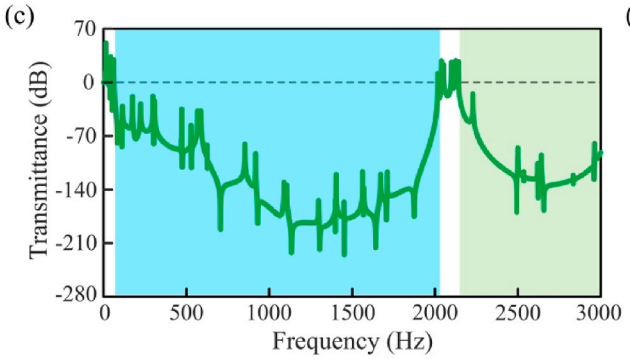

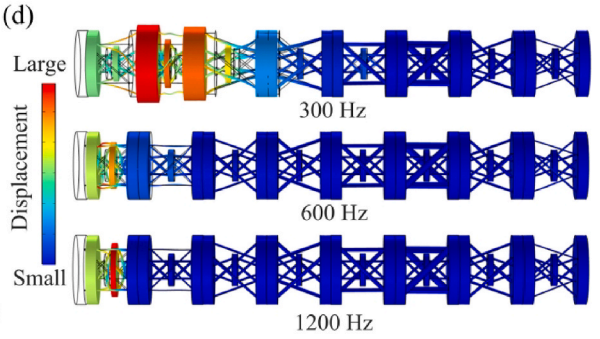

Fig. 15. Vibration suppression enhancement of aperiodic metamaterials via parameter optimization. (a) Normalized bandwidth evolution during the optimization process, achieving a maximum value of 1.87. (b) Resultant optimized parameters of the aperiodic metamaterial with 8 chiral elementary cells. Here, $d_{c,\,i}$ is the radius of external struts for the i-th elementary cell, while $e_{c,\,i}$, $b_{c,\,i}$ and $t_{c,\,i}$ correspond to the chirality of the external frame, bottom internal macrostructure, and top internal macrostructure, respectively. (c) Transmittance spectra of the aperiodic metamaterial after optimization, with the first vibration suppression zone ranging from 63.4 to 2017.3 Hz. (d) Vibration modes of the optimized aperiodic metamaterial at 300 Hz, 600 Hz, and 1200 Hz.

where $\Psi_{\min}$ is the minimal transmittance ratio; w_1 and w_2 are the weighting coefficients for the bandwidth and attenuation amplitude, respectively. To facilitate direct comparison, Ψ_{ref} is introduced as a reference transmittance for normalization. Given that the developed theoretical formulation facilitates efficient calculation of the transmittance spectrum for arbitrary combination configurations, an optimal design can be identified on demand by applying the particle swarm optimization algorithm.

7. Conclusion

In this work, a novel design strategy has been presented for developing periodic and aperiodic hierarchical chiral metamaterials for broadband vibration suppression. The theoretical analyses and technical discussions lead to the following key findings:

(1) The design strategy that combines the principles of "tacticity" and "hierarchy" results in eight chiral elementary cells with self-similar geometries for constructing hierarchical chiral metamaterials. Compared with classic non-hierarchical and mono-hierarchical chiral metamaterials, the developed chiral metamaterial exhibits a lower start frequency at identical stiffness-mass ratios.

(2) The developed theoretical model, rigorously validated through simulational and experimental results, accurately predicts the vibration response and dispersion relation, paving the way to the on-demand customization design of vibration suppression performance of such hierarchical chiral metamaterials.

(3) The comprehensive parametric analysis reveals that the strut diameter of the external frame is more sensitive to the band gap variations than other geometric parameters. Interestingly, the band gap within a specific frequency range can be opened or closed by altering the rotational constraints at each elementary cell, enabling basic logic gate operations.

(4) Through the combination optimization of distinct chirality sequences and non-uniform parameters, the resultant aperiodic hierarchical metamaterial significantly outperforms the standard periodic configuration, exhibiting a 122.2 % increase in suppression bandwidth and a 34.4 % reduction in starting frequency for broadband vibration suppression. This suggests that the aperiodic design approach offers obvious advantages in widening the band gap than traditional periodic designs.

To summarize, this work sheds valuable insights into the vibration suppression capabilities of hierarchical chiral metamaterials, while simultaneously expanding the boundaries of metamaterial properties through the transition from periodic to aperiodic designs.

CRediT authorship contribution statement

Dewen Yu: Writing – review & editing, Writing – original draft, Validation, Supervision, Software, Project administration, Methodology, Investigation, Funding acquisition, Conceptualization. **Qiangqiang Zhao:** Writing – review & editing, Writing – original draft, Visualization, Supervision, Software, Methodology, Investigation, Data curation, Conceptualization. **Gang Wang:** Writing – original draft, Visualization, Validation, Software, Resources, Methodology, Investigation. **Guobiao Hu:** Writing – review & editing, Writing – original draft, Validation, Software, Resources, Formal analysis, Data curation. **Haoxiang Xi:** Visualization, Validation, Methodology, Investigation, Formal analysis, Data curation. **Baiyi Li:** Visualization, Validation, Methodology, Investigation, Formal analysis, Data curation. **Jun Hong:** Writing – original draft, Visualization, Supervision, Software, Resources, Formal analysis.

Declaration of competing interest

The authors declare that they have no known competing financial interests or personal relationships that could have appeared to influence the work reported in this paper.

Acknowledgments

The work is financially supported by the National Natural Science Foundation of China (Grant No. 52405291), the China Postdoctoral Program for Innovative Talents (Grant No. BX20250419), and the Fundamental Research Funds for the Central Universities (Grant No. xzy012025125).

Data availability

No data was used for the research described in the article.

References

[1] P. Jiao, J. Mueller, J.R. Raney, X. Zheng, A.H. Alavi, Mechanical metamaterials and beyond, Nat. Commun. 14 (2023) 6004.
[2] M. Al Rifaie, H. Abdulhadi, A. Mian, Advances in mechanical metamaterials for vibration isolation: a review, Adv. Mech. Eng. 14 (2022), 16878132221082872.
[3] K. Bertoldi, V. Vitelli, J. Christensen, M. Van Hecke, Flexible mechanical metamaterials, Nat. Rev. Mater. 2 (2017) 1–11.
[4] S. Bonfanti, S. Hiemer, R. Zulkarnain, R. Guerra, M. Zaiser, S. Zapperi, Computational design of mechanical metamaterials, Nat. Comput. Sci. 4 (2024) 574–583.
[5] X. Wang, J. Li, Y. Wang, Y. Liu, Active control of wave propagation direction of elastic metamaterial, Eur. J. Mech. A/Solids 113 (2025) 105685.
[6] L. Bai, H. Yao, C. Han, X. Jing, L.-Q. Chen, A.F. Vakakis, T. Yang, Recent advances in nonlinear vibration metamaterials, Mech. Syst. Sig. Process. 236 (2025) 113046.
[7] A. Banerjee, R. Das, E.P. Calius, Waves in structured mediums or metamaterials: a review, Arch. Comput. Meth. Eng. 26 (2019) 1029–1058.
[8] B. Zhao, H.R. Thomsen, X. Pu, S. Fang, Z. Lai, B. Van Damme, A. Bergamini, E. Chatzi, A. Colombi, A nonlinear damped metamaterial: Wideband attenuation with nonlinear bandgap and modal dissipation, Mech. Syst. Sig. Process. 208 (2024) 111079.
[9] J. Ji, Q. Luo, K. Ye, Vibration control based metamaterials and origami structures: a state-of-the-art review, Mech. Syst. Sig. Process. 161 (2021) 107945.

[10] I. Arretche, K.H. Matlack, Centrifugal forces enable band gaps that self-adapt to synchronous vibrations in rotating elastic metamaterial, Mech. Syst. Sig. Process. 202 (2023) 110689.
[11] S. Rui, W. Zhang, R. Yu, X. Wang, F. Ma, A multi-band elastic metamaterial for low-frequency multi-polarization vibration absorption, Mech. Syst. Sig. Process. 216 (2024) 111464.
[12] J. Morris, W. Wang, T. Plaisted, C.J. Hansen, A.V. Amirkhizi, Optimizing graded metamaterials via genetic algorithm to control energy transmission, Int. J. Mech. Sci. 263 (2024) 108775.
[13] E. Nobrega, F. Gautier, A. Pelat, J. Dos Santos, Vibration band gaps for elastic metamaterial rods using wave finite element method, Mech. Syst. Sig. Process. 79 (2016) 192–202.
[14] M. Kadic, G.W. Milton, M. van Hecke, M. Wegener, 3D metamaterials, Nat. Rev. Phys. 1 (2019) 198–210.
[15] L. Wang, J. Boddapati, K. Liu, P. Zhu, C. Daraio, W. Chen, Mechanical cloak via data-driven aperiodic metamaterial design, Proc. Natl. Acad. Sci. 119 (2022) e2122185119.
[16] J.U. Surjadi, L. Gao, H. Du, X. Li, X. Xiong, N.X. Fang, Y. Lu, Mechanical metamaterials and their engineering applications, Adv. Eng. Mater. 21 (2019) 1800864.
[17] Y. Jin, X.-Y. Jia, Q.-Q. Wu, X. He, G.-C. Yu, L.-Z. Wu, B. Luo, Design of vibration isolators by using the Bragg scattering and local resonance band gaps in a layered honeycomb meta-structure, J. Sound Vib. 521 (2022) 116721.
[18] Y. Wu, H. Yao, X. Li, S. Han, Metamaterial shaft with a low Poisson's ratio lattice structure for torsional vibration isolation, Mech. Syst. Sig. Process. 228 (2025) 112454.
[19] G. Wang, S. Wan, J. Hong, S. Liu, X. Li, Enhancement of the vibration attenuation characteristics in local resonance metamaterial beams: theory and experiment, Mech. Syst. Sig. Process. 188 (2023) 110036.
[20] Z. Liu, X. Zhang, Y. Mao, Y.Y. Zhu, Z. Yang, C.T. Chan, P. Sheng, Locally resonant sonic materials, Science 289 (2000) 1734–1736.
[21] O. Yuksel, C. Yilmaz, Realization of an ultrawide stop band in a 2-D elastic metamaterial with topologically optimized inertial amplification mechanisms, Int. J. Solids Struct. 203 (2020) 138–150.
[22] C. Yilmaz, G.M. Hulbert, N. Kikuchi, Phononic band gaps induced by inertial amplification in periodic media, Phys. Rev. B—Condens. Matter Mater. Phys. 76 (2007) 054309.
[23] L. Xu, Z. Yang, Z. Zhang, E. Li, J. Zhou, B. Li, Lightweight composite meta-lattice structures with inertial amplification design for broadband low-frequency vibration mitigation, Compos. B Eng. 292 (2025) 112091.
[24] R. Hamzehei, M. Bodaghi, N. Wu, Mastering the art of designing mechanical metamaterials with quasi-zero stiffness for passive vibration isolation: a review, Smart Mater. Struct. 33 (2024) 083001.
[25] C. Cai, J. Zhou, L. Wu, K. Wang, D. Xu, H. Ouyang, Design and numerical validation of quasi-zero-stiffness metamaterials for very low-frequency band gaps, Compos. Struct. 236 (2020) 111862.
[26] J. Liu, Y. Wang, S. Yang, T. Sun, M. Yang, W. Niu, Customized quasi-zero-stiffness metamaterials for ultra-low frequency broadband vibration isolation, Int. J. Mech. Sci. 269 (2024) 108958.
[27] B. Song, S. Zhang, L. Zhang, Y. Shi, Development trends and challenges of additive manufacturing metamaterials, Engineering 44 (2025) 2–6.
[28] G. Yoon, I. Kim, J. Rho, Challenges in fabrication towards realization of practical metamaterials, Microelectron. Eng. 163 (2016) 7–20.
[29] M.Y. Khalid, Z.U. Arif, A. Tariq, M. Hossain, R. Umer, M. Bodaghi, 3D printing of active mechanical metamaterials: a critical review, Mater. Des. 246 (2024) 113305.
[30] W. Wu, W. Hu, G. Qian, H. Liao, X. Xu, F. Berto, Mechanical design and multifunctional applications of chiral mechanical metamaterials: a review, Mater. Des. 180 (2019) 107950.
[31] W. Jiang, M. Fu, L. Hu, Y. Wang, H. Wu, A novel nested compression-torsion metamaterial with independently customized mechanical properties, Eng. Struct. 322 (2025) 119246.
[32] R. Zhong, M. Fu, X. Chen, B. Zheng, L. Hu, A novel three-dimensional mechanical metamaterial with compression-torsion properties, Compos. Struct. 226 (2019) 111232.
[33] W. Ding, T. Chen, D. Yu, C. Chen, R. Zhang, J. Zhu, B. Assouar, Isotacticity in chiral phononic crystals for low-frequency bandgap, Int. J. Mech. Sci. 261 (2024) 108678.
[34] H. Ou, L. Hu, Y. Wang, C. Liu, High-efficient and reusable impact mitigation metamaterial based on compression-torsion coupling mechanism, J. Mech. Phys. Solids 186 (2024) 105594.
[35] T. Frenzel, M. Kadic, M. Wegener, Three-dimensional mechanical metamaterials with a twist, Science 358 (2017) 1072–1074.
[36] I. Fernandez-Corbaton, C. Rockstuhl, P. Ziemke, P. Gumbsch, A. Albiez, R. Schwaiger, T. Frenzel, M. Kadic, M. Wegener, New twists of 3D chiral metamaterials, Adv. Mater. 31 (2019) 1807742.
[37] X. Fang, D. Yu, J. Wen, Y. Dai, M.R. Begley, H. Gao, P. Gumbsch, Large recoverable elastic energy in chiral metamaterials via twist buckling, Nature (2025) 1–7.
[38] A.H. Orta, C. Yilmaz, Inertial amplification induced phononic band gaps generated by a compliant axial to rotary motion conversion mechanism, J. Sound Vib. 439 (2019) 329–343.
[39] A. Li, Z.-M. Bai, X. Yin, T. Zhu, Z.-Y. Sun, J. Yang, L.-Y. Zhang, A tensegrity-inspired inertial amplification metastructure with tunable dynamic characteristics, J. Mech. Phys. Solids 196 (2025) 106037.
[40] W. Ding, T. Chen, C. Chen, D. Chronopoulos, J. Zhu, B. Assouar, Thomson scattering-induced bandgap in planar chiral phononic crystals, Mech. Syst. Sig. Process. 186 (2023) 109922.
[41] J. Park, G. Lee, H. Kwon, M. Kim, J. Rho, All-polarized elastic wave attenuation and harvesting via chiral mechanical metamaterials, Adv. Funct. Mater. 34 (2024) 2403550.
[42] S. Qu, W. Ding, L. Dong, J. Zhu, S. Zhu, Y. Yang, W. Zhai, Chiral phononic crystal-inspired railway track for low-frequency vibration suppression, Int. J. Mech. Sci. 274 (2024) 109275.
[43] A. Bergamini, M. Miniaci, T. Delpero, D. Tallarico, B. Van Damme, G. Hannema, I. Leibacher, A. Zemp, Tacticity in chiral phononic crystals, Nat. Commun. 10 (2019) 4525.
[44] W. Ding, T. Chen, C. Chen, D. Chronopoulos, B. Assouar, Y. Wen, J. Zhu, Description of bandgaps opening in chiral phononic crystals by analogy with Thomson scattering, New J. Phys. 25 (2023) 103001.
[45] W. Ding, R. Zhang, T. Chen, S. Qu, D. Yu, L. Dong, J. Zhu, Y. Yang, B. Assouar, Origin and tuning of bandgap in chiral phononic crystals, Commun. Phys. 7 (2024) 272.
[46] J. Park, D. Lee, Y. Jang, A. Lee, J. Rho, Chiral trabeated metabeam for low-frequency multimode wave mitigation via dual-bandgap mechanism, Commun. Phys. 5 (2022) 194.
[47] R. Zhang, W. Ding, B. Fang, P. Feng, K. Wang, T. Chen, J. Zhu, Syndiotactic chiral metastructure with local resonance for low-frequency vibration isolation, Int. J. Mech. Sci. 281 (2024) 109564.
[48] D. Yu, G. Wang, Q. Zhao, W. Ding, G. Hu, J. Hong, Isotactic and syndiotactic chiral mechanical metamaterials with tunable band gaps, Mech. Syst. Sig. Process. 230 (2025) 112602.
[49] P. Kudela, A. Ijjeh, M. Radzienski, M. Miniaci, N. Pugno, W. Ostachowicz, Deep learning aided topology optimization of phononic crystals, Mech. Syst. Sig. Process. 200 (2023) 110636.
[50] M. Heshmati, S.K. Jalali, N.M. Pugno, An innovative hierarchical design of hybrid meta-structures for longitudinal waveguides, Int. J. Mech. Sci. 287 (2025) 109963.
[51] X. Wang, Z. Liang, Z. Tang, S. Rui, K. Li, F. Ma, On-demand design for elastic metamaterial based on a semi-analytical band gap rapid extraction method, Mater. Horiz. 12 (2025) 4289–4303.
[52] D. Yu, G. Hu, W. Ding, Y. Yang, J. Hong, Zero-thermal-expansion metamaterial with broadband vibration suppression, Int. J. Mech. Sci. 258 (2023) 108590.

[53] Z. Wu, W. Liu, F. Li, C. Zhang, Band-gap property of a novel elastic metamaterial beam with X-shaped local resonators, Mech. Syst. Sig. Process. 134 (2019) 106357.
[54] J. Wang, J. Callanan, O. Ogunbodede, R. Rai, Hierarchical combinatorial design and optimization of non-periodic metamaterial structures, Addit. Manuf. 37 (2021) 101710.
[55] G. Hu, A.C. Austin, V. Sorokin, L. Tang, Metamaterial beam with graded local resonators for broadband vibration suppression, Mech. Syst. Sig. Process. 146 (2021) 106982.
[56] A. Banerjee, Flexural waves in graded metabeam lattice, Phys. Lett. A 388 (2021) 127057.
[57] M.V. Barnhart, X. Xu, Y. Chen, S. Zhang, J. Song, G. Huang, Experimental demonstration of a dissipative multi-resonator metamaterial for broadband elastic wave attenuation, J. Sound Vib. 438 (2019) 1–12.
[58] D. Yao, M. Xiong, J. Luo, L. Yao, Flexural wave mitigation in metamaterial cylindrical curved shells with periodic graded arrays of multi-resonator, Mech. Syst. Sig. Process. 168 (2022) 108721.
[59] O. Abdeljaber, O. Avci, D.J. Inman, Optimization of chiral lattice based metastructures for broadband vibration suppression using genetic algorithms, J. Sound Vib. 369 (2016) 50–62.
[60] C. Gomes, M. dos Santos, B. Araújo, F. Pereira, E. Nobrega, J. Dos Santos, E. Miranda Jr, A. Sinatora, Wave and vibration attenuation in graded elastic metamaterial beams with local resonators, Int. J. Mech. Sci. 293 (2025) 110125.
[61] M. Alshaqaq, C. Sugino, A. Erturk, Programmable rainbow trapping and band-gap enhancement via spatial group-velocity tailoring in elastic metamaterials, Phys. Rev. Appl 17 (2022) L021003.
[62] H. Meng, N. Bailey, Y. Chen, L. Wang, F. Ciampa, A. Fabro, D. Chronopoulos, W. Elmadih, 3D rainbow phononic crystals for extended vibration attenuation bands, Sci. Rep. 10 (2020) 18989.
[63] C. Li, T. Jiang, Q. He, Z. Peng, Stiffness-mass-coding metamaterial with broadband tunability for low-frequency vibration isolation, J. Sound Vib. 489 (2020) 115685.
[64] J. Li, Y. Zhang, X. Fan, F. Li, Multi bandgaps design of sandwich metamaterial plate with embedded membrane-type resonators, J. Sandwich Struct. Mater. 25 (2023) 311–329.
[65] V.F. Dal Poggetto, F. Bosia, M. Miniaci, N.M. Pugno, Band gap enhancement in periodic frames using hierarchical structures, Int. J. Solids Struct. 216 (2021) 68–82.
[66] K. Wu, H. Hu, L. Wang, Y. Gao, Parametric optimization of an aperiodic metastructure based on genetic algorithm, Int. J. Mech. Sci. 214 (2022) 106878.
[67] C. Lim, Z. Yaw, Z. Chen, Periodic and aperiodic 3-D composite metastructures with ultrawide bandgap for vibration and noise control, Compos. Struct. 287 (2022) 115324.
[68] S. Timorian, M. Ouisse, N. Bouhaddi, S. De Rosa, F. Franco, Numerical investigations and experimental measurements on the structural dynamic behaviour of quasi-periodic meta-materials, Mech. Syst. Sig. Process. 136 (2020) 106516.
[69] A. Li, Y. Fan, Y. Wu, L. Li, K. Yi, Retuning the disordered periodic structures by sorting unit cells: Numerical analyses and experimental studies, J. Sound Vib. 566 (2023) 117925.
[70] X. Pu, A. Palermo, A. Marzani, Topological edge states of quasiperiodic elastic metasurfaces, Mech. Syst. Sig. Process. 181 (2022) 109478.
[71] H. Tang, Z. Hao, Y. Liu, Y. Tian, H. Niu, J. Zang, Soft and disordered hyperuniform elastic metamaterials for highly efficient vibration concentration, Natl. Sci. Rev. 9 (2022) nwab133.
[72] D. Yu, G. Hu, Z. Guo, J. Hong, Y. Yang, Topological interface state formation in an hourglass lattice sandwich meta-structure, Int. J. Mech. Sci. 246 (2023) 108170.
[73] M. Nieves, A. Movchan, Meso-scale method of asymptotic analysis of elastic vibrations in periodic and non-periodic multi-structures, Quart. J. Mech. Appl. Math. 75 (2022) 171–214.
[74] H. Zhu, S. Patnaik, T.F. Walsh, B.H. Jared, F. Semperlotti, Nonlocal elastic metasurfaces: Enabling broadband wave control via intentional nonlocality, Proc. Natl. Acad. Sci. 117 (2020) 26099–26108.
[75] A. Glacet, A. Tanguy, J. Réthoré, Vibrational properties of quasi-periodic beam structures, J. Sound Vib. 442 (2019) 624–644.
[76] Z. Wang, Q. Zhang, K. Zhang, G. Hu, Tunable digital metamaterial for broadband vibration isolation at low frequency, Adv. Mater. 28 (2016) 9857–9861.
[77] L. D'Alessandro, A.O. Krushynska, R. Ardito, N.M. Pugno, A. Corigliano, A design strategy to match the band gap of periodic and aperiodic metamaterials, Sci. Rep. 10 (2020) 16403.
[78] M. Zaiser, S. Zapperi, Disordered mechanical metamaterials, Nat. Rev. Phys. 5 (2023) 679–688.
[79] M. Mirzaali, R. Hedayati, P. Vena, L. Vergani, M. Strano, A. Zadpoor, Rational design of soft mechanical metamaterials: Independent tailoring of elastic properties with randomness, Appl. Phys. Lett. 111 (2017).
[80] Y. Li, G. Yin, G. Yan, S. Yao, Forward-backstepping design of phononic crystals with anticipated band gap by data-driven method, Mech. Syst. Sig. Process. 224 (2025) 111975.
[81] Z. Zhou, A.M. LaPointe, G.W. Coates, Atactic, isotactic, and syndiotactic methylated polyhydroxybutyrates: an unexpected series of isomorphic polymers, J. Am. Chem. Soc. 145 (2023) 25983–25988.
[82] J. Zhang, X. Peng, D. Yu, G. Hu, Y. Yang, Rigid-elastic combined metamaterial beam with tunable band gaps for broadband vibration suppression, J. Vib. Acoust. 146 (2024) 021004.
[83] V.F. Dal Poggetto, A.L. Serpa, Flexural wave band gaps in a ternary periodic metamaterial plate using the plane wave expansion method, J. Sound Vib. 495 (2021) 115909.
[84] P. Zhao, K. Zhang, L. Qi, Z. Deng, 3D chiral mechanical metamaterial for tailored band gap and manipulation of vibration isolation, Mech. Syst. Sig. Process. 180 (2022) 109430.
[85] G. Hu, L. Tang, Y. Yang, D. Yu, Y. Zi, High-fidelity dynamics of piezoelectric covered metamaterial Timoshenko beams using the spectral element method, Smart Mater. Struct. 32 (2023) 095023.
[86] R. Sinha, T.V. Varma, S. Sarkar, Effect of nonlocality on the dispersion relations of mechanical metamaterials, Int. J. Mech. Sci. 279 (2024) 109489.
[87] C. Yin, Y. Xiao, Z. Zhang, Q. Qin, Y. Liu, Design framework for phononic crystals based on compression-twist coupling structures with curved beams, Int. J. Mech. Sci. 266 (2024) 108920.
[88] D. Yu, G. Hu, S. Cai, Y. Yang, J. Hong, Active optimization adjustment for the surface accuracy of spaceborne SAR antennas, Aerosp. Sci. Technol. 138 (2023) 108330.